Four-Wave Mixing with Orbital Angular Momentum Transfer

A thesis submitted in partial fulfillment of the requirement for the degree of

Bachelor of Science in Physics from The College of William and Mary,

by

Hana K. Warner

Accepted for: _____ Honors
(Honors or no-Honors)

_____
Irina Novikova, Advisor
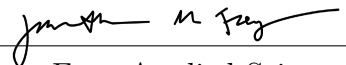
_____
Jonathan Frey, Applied Sciences

_____
Keith Griffieon, Physics

Williamsburg, Virginia
May 1, 2020

Contents

Acknowledgments

I would like to thank Professor Irina Novikova for her endless support and encouragement over the past several years. Thank you for introducing me to the world of optics and challenging me to go further and understand more in physics: your support has genuinely changed my life. Thank you to Kanging Yang, who I have collaborated with for the past three years and who I started building this experiment with two years ago. This work would be impossible without you. Thank you to Nik Prajapati, Savannah Cuozzo, and Professor Euginey Mikhailov for your help and guidance and the William and Mary Quantum Optics group for their support. You all have made the past four years a blast and are an inspiration in your research and outreach efforts.

Finally, I would like to thank my friends and family for their support. I would not have gotten to this point without you.

List of Figures

Abstract

We explore the conservation of orbital angular momentum (OAM) in the four-wave mixing (FWM) process in hot rubidium vapor. Since most modern communication systems send data in pulses corresponding to bits, we can use OAM to encode more information in each pulse by assigning structure to each signal. Furthermore, because FWM can be used to generate entangled photon pairs, we can use this process to bring enhanced signal security. We experimentally studied FWM with a wide range of Laguerre-Gaussian modes and their superpositions and observed OAM transfer from the probe field to a generated Stokes field. By studying the output Stokes intensity and phase distributions, we confirm ℓ mode (OAM) conservation for pure ℓ and p modes, as well as for the superpositions of ℓ and $-\ell$ for the mode numbers up to $\ell = 4$, $p = 4$. We also found that p index is generally not conserved and its conservation is highly dependent on the relative sizes of the probe and pump beams in the Rb cell. We also identify parameters to improve FWM gain with OAM transfer and propose an analytical method for determining OAM p number.

Chapter 1

Introduction

Conventional computer systems send information as electric signals. These signals, called bits, switch on and off in order to convey a message. The message speed depends on how fast electrical pulses can move through a cable. However, it is possible to use light instead of electrons to send more information at once and send that information faster. This is because, rather than using electrons, we can send information in the amplitude and phase of light. Currently, fiber optic communication (Figure 1.1) is used to allow more rapid information transfer by sending pulses of light through an optical fiber [1]. However, light can also carry orbital angular momentum (OAM), which can be used to transmit information even more efficiently by encoding each photon with different OAM to give each signal a different meaning [2].

Figure 1.1: Information can be sent as pulses of light through optical fibers. An electrical signal will trigger a transmitter, usually a laser or diode, and a receiver will collect the signal and transform it back into an electrical signal.

Additionally, entangled quantum states can be used to prevent eavesdropping because any unauthorized measurement will affect the quantum state of the system. Entanglement, described by Albert Einstein as "spooky action at a distance," occurs when the state of two objects cannot be described independently of the other, even if they undergo large spatial separation. This results in increased

transmission security and in a low error threshold that requires the receiver to know how to properly measure the incoming signals in order to be able to understand the message [3].

During my undergraduate research, I have demonstrated that information can be encoded into beams of light via OAM and that this information can be transferred to a new field via a nonlinear interaction called four-wave mixing (FWM) due to energy and momentum conservation. Since FWM results in the generation of a new field correlated with an input field, any disruptions between them will result in a loss of information and can be used to ensure the security of the quantum transmission.

Four-wave mixing is a process where two or three light fields interact with atoms and produce one or two new fields, as shown in Figure 1.2 [4]. In our configuration, there are two fields, a pump and a probe, that interact and produce a third field, the Stokes.
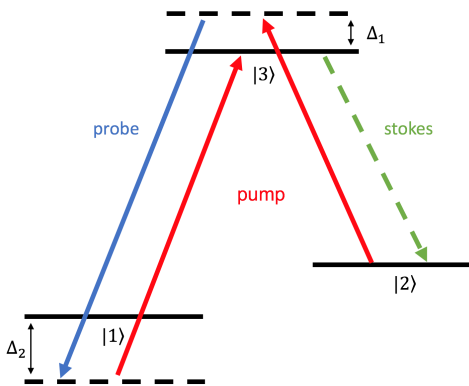
Figure 1.2: Traditional four-wave mixing configuration. The pump and probe interact to produce the Stokes.

Frequency and phase matching conditions are important for this process, so a single laser separated into two polarizations is utilized to control these properties. By using a single source, there is a greater frequency stability, so only the angle at which the fields interact within the medium, ^{87}Rb, and the polarization of the fields need to be matched. The four-wave mixing process must also obey the conservation of orbital angular momentum (OAM). The phase of light rotates as it propagates, and this OAM must be transferred between fields.

2

OAM conservation can also be used to improve imaging techniques. Classical imaging is used for defense and medicine to image things like planes and body systems [5]. However, image resolution, clarity, and functionality are limited by things such as smoke, turbulence, obstructions, and radiation exposure [6]. Quantum imaging utilizes photon entanglement to subvert these barriers and allow for clear imaging in situations where classical images would be distorted or unobtainable. As a result, entangled photons can be used to generate an image from an object where the probing photon never interacted with the object, allowing for greater freedom in analyzing light-sensitive objects [7]. This technique can distinguish between decoy and camouflaged aircrafts, provide inexpensive medical imaging, and allow for nanoscale understanding of active biosystems [8].

Chapter 2

Theory

This section will explore the theory of four-wave mixing and orbital angular momentum.

2.1 Interaction of Light and Atoms

Light and atoms most frequently interact through photon absorption and emission. When light is absorbed by an atom, it can excite electrons into a higher energy state. When atoms re-emit photons, electrons must drop down to a lower energy state. This energy difference $\Delta\mathcal{E}$ between possible atomic states is given defined by

$$\Delta\mathcal{E} = \hbar\omega \tag{2.1}$$

where ω is the light frequency [9].

Resonant light-atom interactions give rise to a number of interesting phenomena. For this project, we are most interested in exploring the phenomenon of four-wave mixing (FWM).

2.2 Four-Wave Mixing

Four-wave mixing (FWM) is a process where two electromagnetic fields interact in a nonlinear medium to produce one or two new fields and depends on the electric susceptibility of the medium [10]. It can be used to generate correlated photon pairs or entangled photons.

Most fields are plane waves, which are defined as

$$\mathbf{E} = E_0(z,t)e^{-i\omega t + i\mathbf{kz}}\mathbf{e_{pol}} \tag{2.2}$$

where E_0 is the electric field, z is the propogation distance, t is time, ω is the light frequency, k is the wave number, and e_{pol} is the polarization vector. The nonlinearity of an optical medium is traditionally described by different orders of susceptibility parameters $\chi^{(i)}$ defined as

$$\mathbf{P(t)} = \epsilon_0(\chi^{(1)}\mathbf{E(t)} + \chi^{(2)}\mathbf{E^2(t)} + \chi^{(3)}\mathbf{E^3(t)}) \tag{2.3}$$

where P(t) is defined as the dielectric polarization density.
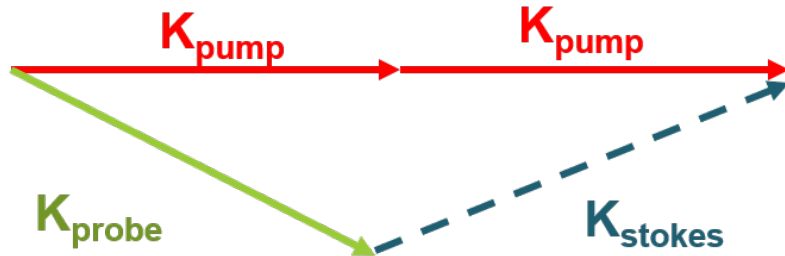
Figure 2.1: Energy is conserved during FWM

The FWM process is caused by the third order nonlinear susceptibility $\chi^{(3)}$. The generated field is called the Stokes field, and its amplitude (E_{Stokes}) is proportional to

the medium polarization at the frequency of the stokes field (P_{Stokes}) and is related to the pump and probe amplitudes as

$$\frac{dE_{Stokes}}{dz} \sim P_{Stokes} = \epsilon_0 \chi^{(3)}_{FWM} (E_{pump})^2 E^*_{probe} \tag{2.4}$$

Generation of the new field results from energy and momentum conservation (Figure 2.1), so for an interaction between two laser fields, called the pump and the probe, one with frequency ω_{pump} and wave vector $\mathbf{k_{pump}}$ and the other with frequency ω_{probe} and wave vector $\mathbf{k_{probe}}$, the output frequency will be

$$\omega_{Stokes} = 2\omega_{pump} - \omega_{probe} \tag{2.5}$$

with wave vector

$$\mathbf{k_{Stokes}} = 2\mathbf{k_{pump}} - \mathbf{k_{probe}} \tag{2.6}$$
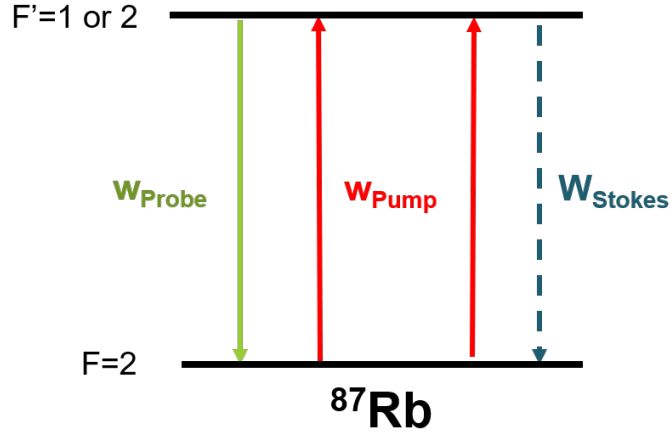
Figure 2.2: Our four-wave mixing configuration, where the pump and probe are degenerate.

This is because two photons are used from the first field, while one photon is used from the second field in order to generate the new field, called the Stokes [11]. For this project, we are studying degenerate FWM, so the frequencies of the pump and probe

fields are identical, and the energy conservation is automatically satisfied (Figure 2.2).

This FWM interaction can occur in crystalline structures or within atomic vapor; for this project, we are studying four-wave mixing interactions within ^{87}Rb because Rubidium has a single valance electron. This means that we can optically align spin in order to generate strong coherent resonant interactions, rather than weaker non-resonant, incoherent, spontaneous interactions [12]. For this rubidium isotope, optimal FWM occurs at the $5S_{1/2}F = 2 \rightarrow 5P_{1/2}F' = 2$ or $5S_{1/2}F = 2 \rightarrow 5P_{1/2}F' = 1$ transition.

2.3 Orbital Angular Momentum

Most conventional electromagnetic fields travel as plane waves; this means that each "slice" of the beam has a uniform intensity distribution. Gaussian beams are plane waves that have Gaussian intensity profiles, and are thus most intense at the center. Plane waves can be described as

$$\mathbf{E(r)} = \mathbf{E_0}e^{\pm i\mathbf{k}\cdot\mathbf{r}} = \mathbf{E_0}e^{\pm i\mathbf{k_x x + k_y y + k_z z}} \tag{2.7}$$

And Gaussian beams have an electric field given by

$$\mathbf{E}(r, z) = E_0\hat{x}\frac{w_0}{w(z)}e^{\frac{-r^2}{w(z)^2}}e^{-ikz+k\frac{r^2}{2R(z)}-\psi(z)} \tag{2.8}$$

Where E_0 is the amplitude of the electric field, w_0 is the beam waist, z is the distance from the beam's focus, k is the wave number, $R(z)$ is the radius of curvature, and $\psi(z)$ is the Guoy phase.

However, light can also carry orbital angular momentum in ℓ modes, or a twisting behavior with helical phase. Both plane waves and waves with OAM are shown in Figure 2.3. This behavior is described as a vortex because there is a phase singularity, or

absence of light, in the center of the beam's structure due to destructive interference along the central axis. They can also be described by a topological charge, which defines the number of twists the light undergoes within one wavelength [13]. Unlike plane waves, a "slice" of a beam carrying nonzero OAM will have the appearance of a torus.
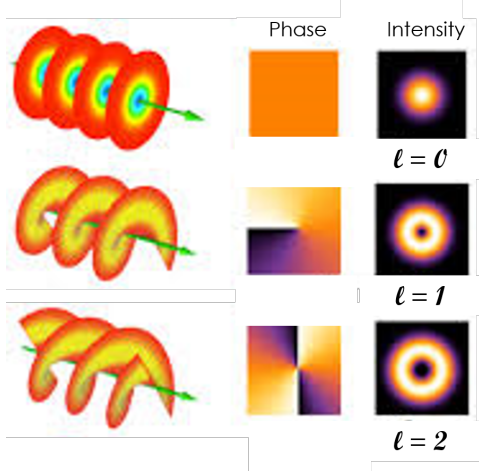
Figure 2.3: Plane waves carry OAM $\ell = 0, 1, 2$. Light with nonzero OAM have helical behavior and complete ℓ cycles within one wavelength.

Meanwhile, p modes describe the radial distribution of light. These mode structures appear centered as rings with interchanging phases. An increase in the p index results in p additionally rings around the central axis. LG modes are defined as

$$LG_p^\ell = \frac{C_p^\ell}{w}\left(\frac{r\sqrt{2}}{w}\right)^{|\ell|} L_p^{|\ell|}\left[\frac{2r^2}{w^2}\right] e^{-\frac{r^2}{w^2}+i(kz+\ell\theta+\Phi)} \tag{2.9}$$

where w is the beam waist, $L_p^{|\ell|}$ is the Laguerre polynomial, r is the radial distance from the center of the beam, z is the axial distance from the beam's waist, and Φ is the sum of the generalized phase front and Guoy phase. The ℓ and p modes form an infinite dimensional basis on which we can encode information (Figure 2.4).

8
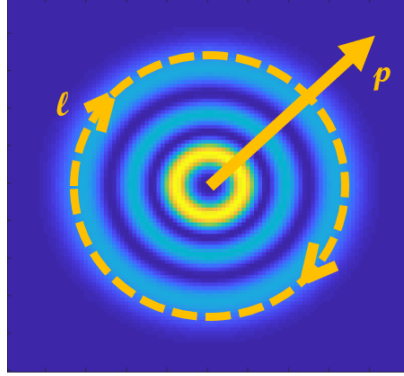
Figure 2.4: An $\ell = 2, p = 2$ Laguerre Gaussian beam. Laguerre Gaussian beams can be described by their azimuthal ℓ number and radial p number. The radial number describes the number of dark rings around the center of the beam, and the azimuthial number describes the hole at the center of the beam.

The ℓ number is difficult to determine from only looking at the image of the beam. However, p index can be determine by counting the number of dark fringes; the number of fringes should be equal to the p number.

Azimuthal ℓ and radial p modes can exist independently, or in superpositions of fields with ℓ and p modes present (Figure 2.5).
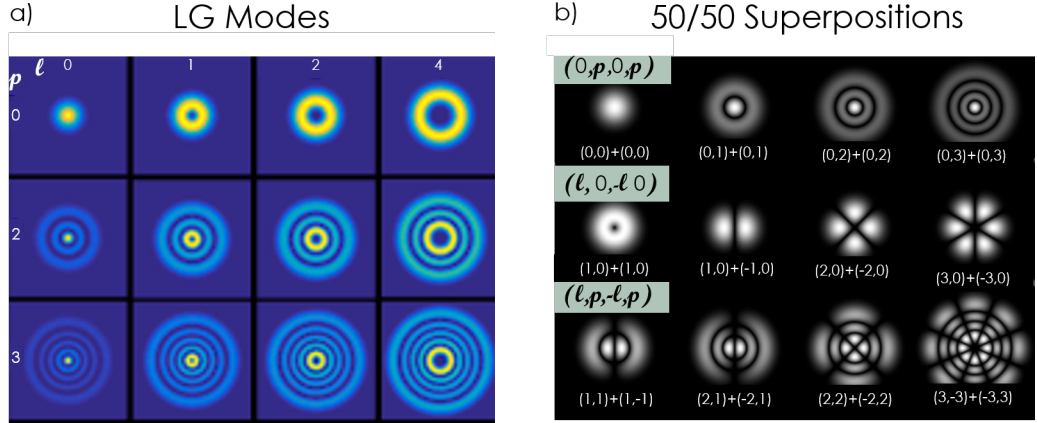
Figure 2.5: Examples of fields with OAM. In (a), we see fields with only azimuthial OAM (row 1), fields with only radial OAM (column 1) and fields with both azimuthial and radial OAM. in (b), we see fields with superpositions of OAM. Row 1 demonstrates superpositions of equal radial OAM with no azimuthial OAM. Row 2 demonstrates fields with azimuthial OAM but no radial OAM. Row 3 shows fields with superpositions of fields with equal p numbers and equal and opposite ℓ numbers.

When we have a superposition of fields with OAM, we see that uniform p numbers add to create a field that is identical to the two original fields. This is because there is no phase change, and therefore no cancellations leading to different structures in the electric field. However, because the phases of the modes with opposite OAM are twisting in opposite directions, when we combine them we see an interference that arises to a petal-like structure with twice as many petals as ℓ number due to the number of twists that occur within one wavelength.

OAM is conserved during four-wave mixing [14]. These conservation laws can all be derived from Equation 2.4. Since

$$E_{pump} \sim e^{i\ell_{pump}\phi} \tag{2.10}$$

and

$$E_{probe} \sim e^{i\ell_{probe}\phi} \tag{2.11}$$

it follows from equation 2.4 that

$$E_{Stokes} \sim e^{i(2\ell_{pump} - \ell_{probe})\phi} \tag{2.12}$$

thus, the OAM of our Stokes field is

$$\ell_{stokes} = 2\ell_{pump} - \ell_{probe} \tag{2.13}$$

For our configuration, we have nonzero OAM on our probe field while our pump field is a plane wave ($\ell = 0$), and thus

$$\ell_{Stokes} = -\ell_{probe} \tag{2.14}$$

Chapter 3

Experimental Arrangement

3.1 Transverse Optical Mode Generation

We use a spatial light modulator (SLM) to generate Laguerre-Gaussian modes on the probe field. The SLM has a liquid crystal display that we can program in MATLAB to selectively reflect light to induce phase or generate images on our beam (Figure 3.1).
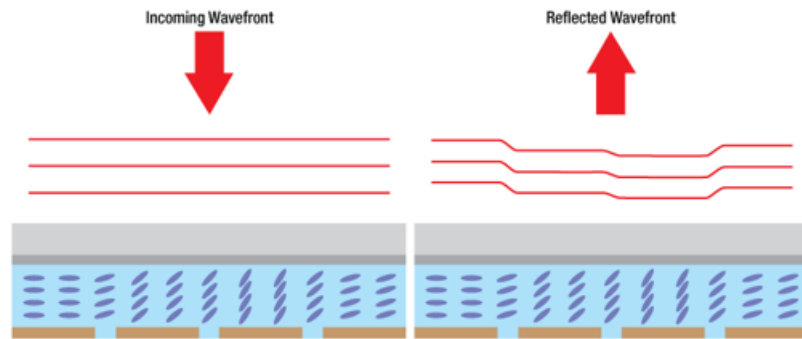
Figure 3.1: The liquid crystal display on our SLM can be programmed to reflect light with different phases. From Thorlabs, Inc.

We can put a flat phase masks on the SLM to reflect plane waves or use a phase mask to induce ℓ modes, p modes, or a superposition of ℓ and p modes as defined in Section 2.3. We can also use the SLM to image more complex objects, such as the William & Mary Cypher and the faces of graduate students in our group, as shown

in Figure 3.2.
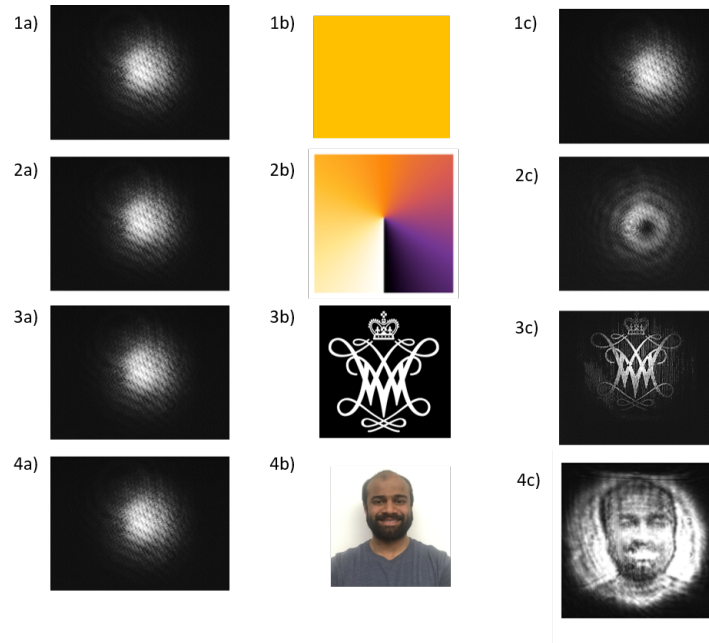
Figure 3.2: Phase masks on our SLM (b) can transform a plane wave (a) into a more complex beam (c).

We are also able to use the SLM as a Fresnel lens by modulating how light is reflected to adjust the focus of the probe field relative to the cell or other optics in our setup.

In order to reliably produce LG modes on our probe field, we first need to determine the position of our beam on the SLM and its intensity profile. This is done by putting a flat mask on our SLM and sequentially turning pixels on and off and measuring the total reflection on a photodiode. The photodiode measures zero power when pixel groups are not reflecting any of our beam, and should otherwise measure a Gaussian profile when the corresponding pixels are turned on and reflecting our beam. If the profile is not perfectly Gaussian, or the beam is not in the center

13

of the SLM, our MATLAB program is adjusted accordingly in order to ensure our phase mask is being applied correctly using the measured intensity profile and Fourier transformation of our beam (Figure 3.3). Finally, when applying the phase mask, we choose a corresponding beam waist for our beam. This is because, since the beam expands for larger ℓ and p modes, the phase mask needs to be condensed in order for the entire beam to pick up phase changes.
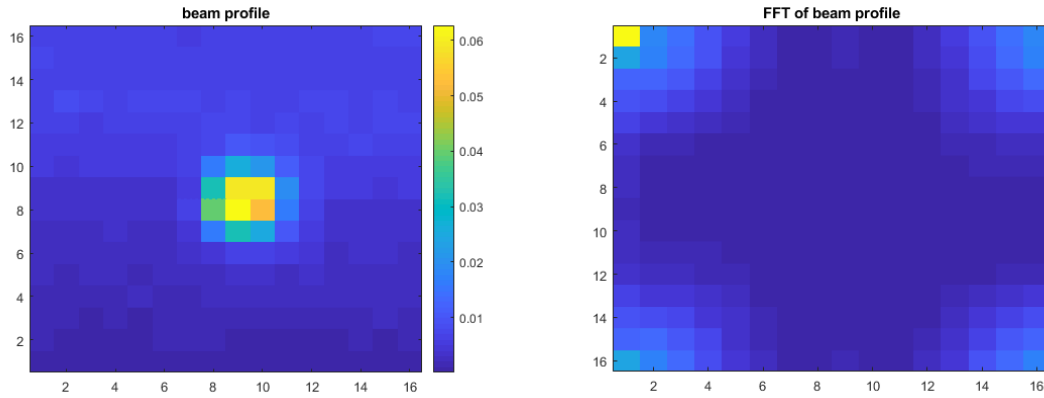
(a) Our beam profile.

(b) The Fourier transformation of our beam.

Figure 3.3: The beam profile and Fourier transform of our beam are used to calibrate our mode generation. Our beam is not perfectly Gaussian and off-center on our SLM screen. However, we can use this profile to apply our correction to our phase mask to get clean LG modes.

3.2 Experimental Setup
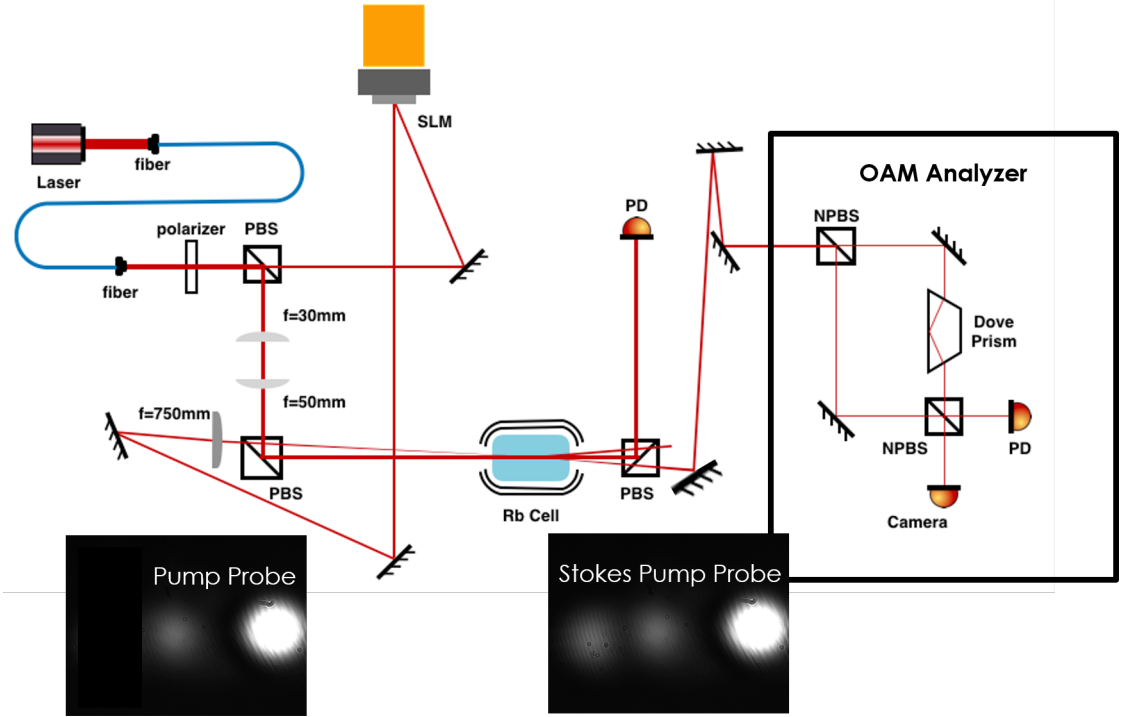
Figure 3.4: A schematic of our experiment. The polarizer separates our laser beam into two fields with different polarizations. The transmitted field is our probe field and the reflected field is our pump field. The probe field is sent to our SLM and then focused by a 750 mm lens before intersecting with our pump field in our cell of Rb atoms. We then use a polarizing beam splitter to separate the Stokes and Probe field from the Pump field, and an edge mirror to send only our Stokes field to our OAM analyzer setup.

Our experimental setup is shown in Figure 3.4. A single laser is separated into a pump and probe field after traveling through a polarizer and then polarizing beam splitter. The polarizer allows us to tune the relative intensity between the pump and probe fields. After separation, the probe field is sent to the SLM where we can either reflect it as a plane wave or program the SLM to induce a phase on the probe. The pump field, meanwhile, is expanded via a telescope to ensure that the pump is larger than the probe even for large ℓ.

15

Phase matching conditions are very important for four-wave mixing. After the SLM, we send the probe to two alignment mirrors before it is recombined with the pump. This allows us to more easily make corrections if the SLM height is not exactly the same as the pump and gives us more freedom in tuning the angle between the pump and probe fields. This is also why we use a polarizing beam splitter to reflect the pump; because the pump and probe are in orthogonal polarizations, we can use the beamsplitter as a mirror for the pump while the probe should be transmitted through it entirely. Thus, we can tune the angle between the pump and probe to be as small as necessary without needing to worry about clipping on the edge of an optic. There is also space to insert a lens on the probe field to focus it at the center of the cell so that the probe remains much smaller than the pump. The probe is amplified by the pump during four-wave mixing, and during this process the Stokes is also generated. Since we are using Gaussian fields, if the pump is not significantly large than the probe then we can have nonuniform amplification and Stokes generation or lose information transmitted at the edges of the field (such as in radial p modes).

The pump and probe are then sent into the cell where they can interact. After the cell, we have a polarizer in place to cut out as much of the pump as possible because it is much stronger than the probe and Stokes fields. The remaining pump, probe, and generated Stokes field are then sent to a photodetector or to a camera in order to measure our fields. The Stokes field can also be diverted to the OAM analyzer so that we can determine the ℓ number. This will be described in further detail in Chapter 4.

3.3   Optimization of Conditions
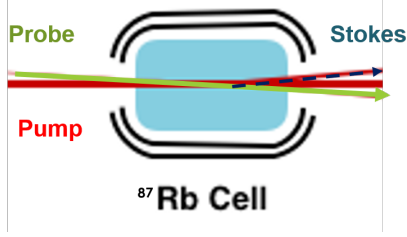
Figure 3.5: Our FWM configuration. The pump and probe intersect inside our Rb cell to produce the Stokes via FWM.

For our experiment, we are studying degenerate four-wave mixing in ^{87}Rb. In order to optimize four-wave mixing, we tune the angle at which the pump and probe intersect inside the Rb cell and then optimize the laser frequency to have the strongest FWM possible (Figure 3.5). Figure 3.6(a) shows that the image of all three optical fields after cell (pump is strongly attenuated). This is done by first optimizing the alignment of the beams while scanning the laser around the $F = 2 \rightarrow F' = 1$ or $F' = 2$ transition and then locking the laser to the frequency corresponding to the strongest Stokes signal. Figure 3.6(b) shows the power of the Stokes field as the laser frequency sweeps through the $F = 2 \rightarrow F' = 1, 2$ transition.
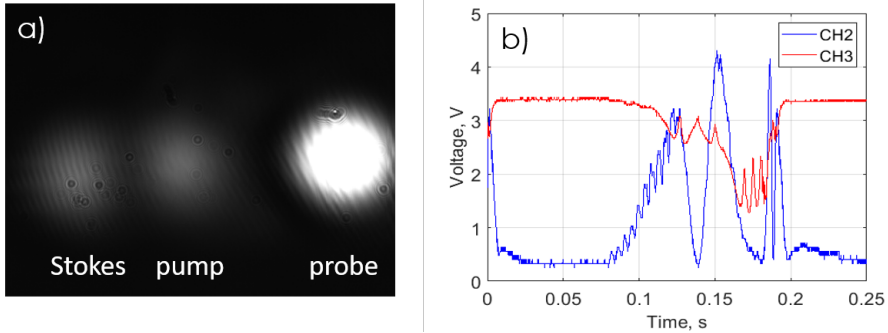
Figure 3.6: (a) Our Stokes, pump, and probe fields when FWM is generated. (b) Stokes power (blue) and Rb reference cell absorption (red) as functions of laser frequency (changing in time).

We also determined that linear probe polarization perpendicular to the linearly polarized pump yielded optimal four-wave mixing (Figure 3.7b) and optimal four-wave mixing occurred at the $F = 2 \rightarrow F' = 1$ transition (Figure 3.7a).
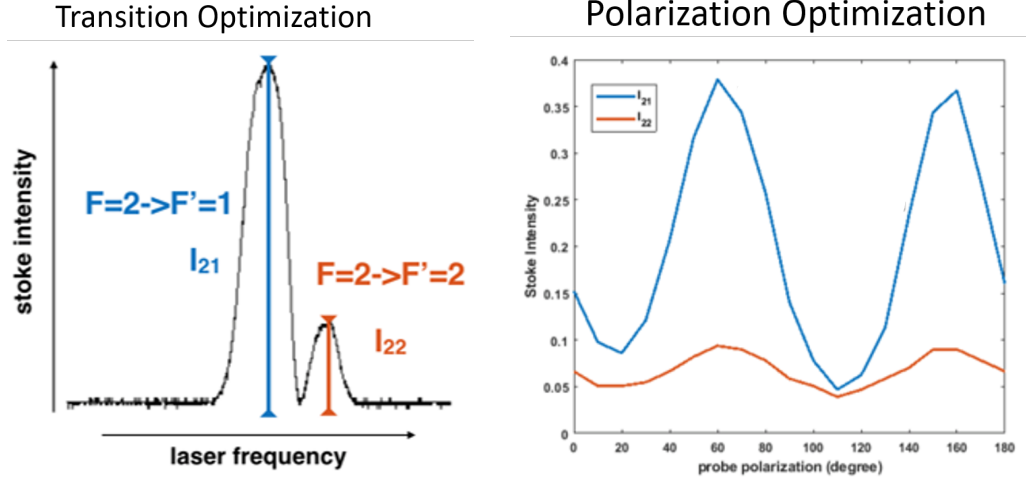
(a) We observed strongest Stokes generation at the $F = 2 \rightarrow F' = 1$ transition.

(b) We observed strongest Stokes generation with linear polarization.

Figure 3.7: Transition and Polarization Optimization

We initially began the experiment using a 7.5cm natural abundance Rubidium cell (meaning that it contains both ^{87}Rb and ^{85}Rb). However, after failing to see Stokes generation with tight focusing in the 7.5 mm cell (briefly discussed in Section 3.3), we proceeded to conduct our experiments with a shorter 2.5 cm cell. Stokes generation with only ℓ modes and an unfocused probe was conducted in the longer 7.5 mm cell at 69^oC (Figure 3.8a), while Stokes generation with p modes and focused probe fields was conducted using the shorter 2.5 mm cell at 90^oC (Figure 3.8b).

Temperature Optimization with 7.5 cm cell

Temperature Optimization with 2.5 cm cell
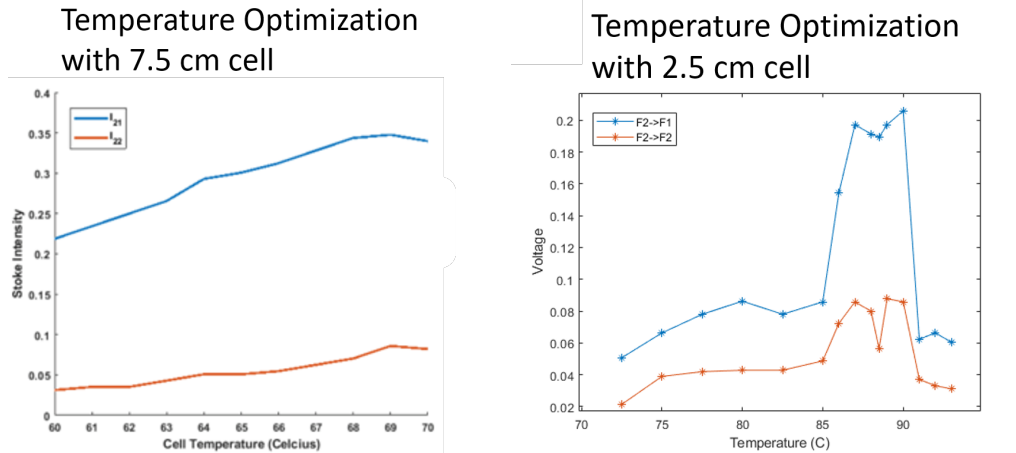
(a) With the longer cell, we had strongest FWM gain at 69^oC.

(b) With the longer cell, we had strongest FWM gain at 90^oC.

Figure 3.8: Temperature Optimization

We suspect that the longer cell has a lower optimal temperature since, as temperature increases, there are more atoms to interact with light. However, in the longer cell, the presence of atoms becomes detrimental to, rather than increasing, our signal since there are more atoms present to absorb light. The dip in Stokes intensity around 87.5^0C is unusual; however, it could be due to fluctuations that occurred while changing temperature or some other phenomena.

3.4 ℓ-Mode Generation

For the first part of our experiment, we studied a configuration where we induced OAM in ℓ modes on the probe field using a phase mask and a 750 mm lens to focus the probe at the center of the cell (where it mixed with the pump field). We also installed a telescope on the pump field to magnify it 1.67x in order to ensure that the pump field is larger than the probe even for large ℓ so that the pump and probe fields mixed effectively. We were able to observe the generation of a Stokes field due to FWM and see transfer of OAM from the probe field to the Stokes field (shown in

19

Figure 3.9). In 1-6(a), we see the structure of the probe field before any interactions occur. In 1-6(b), we see the pump and probe after interacting with Rubidium while the frequency is off resonance so no FWM occurs. In 1-6(c), we see the pump, probe, and Stokes after the cell when the laser is tuned to a frequency where FWM occurs and OAM is transferred from the probe to Stokes.
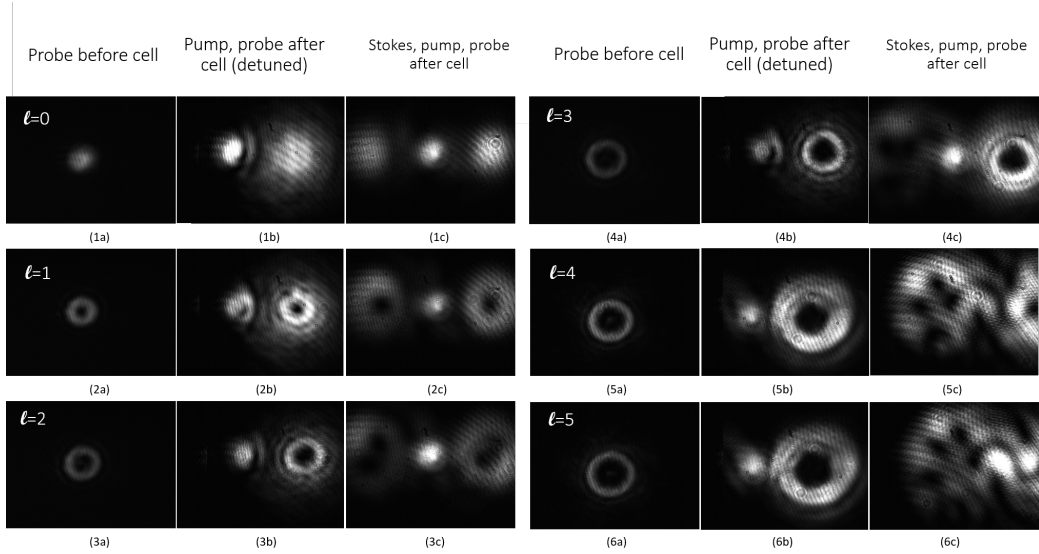
Figure 3.9: We successfully generated a Stokes field via FWM, and saw the transfer of OAM from the probe field to the Stokes field. ℓ=0 to ℓ=5 OAM (1-6) are shown on the probe field when the pump field is blocked (a), the pump and probe off resonance (where no FWM occurs) (b) and when OAM is transfered to the Stokes field via FWM (c).

We can clearly see that the Stokes beam is generated with $\ell \neq 0$ OAM. However, it is difficult to distinguish what modes we are generating when only looking at the image of the beam. In order to have a more robust way to classify our fields, we introduced an OAM analyzer, described in Chapter 4.

3.5   FWM Lens Optimization

We briefly explored FWM behavior when the pump and probe were focused tightly in our cell of Rubidium vapor to determine if we could generate p modes

due to the Gouy phase, a phase shift that results from the propagation of focused Gaussian beams. This was done with a 250mm lens in order for our beam waist, $w = w_0(1 + z/z_R)$ to be the e^{-2} radius in the Raleigh range, $z_R = \pi w_0^2/\lambda$. The generation of this additional phase was observed by a group at the University of Glasgow and the University of Strathclyde [16]. However, we were unable to generate four-wave mixing with the configuration, possibly due to different phase matching conditions between non-degenerate and degenerate four-wave mixing and a different angular configuration.

We also explored conservation of ℓ and p modes when the probe is focused less tightly (Figure 3.11a). We have modified our setup slightly to put a telescope on both the pump and probe so that we can use a greater surface area of the SLM without introducing a phase shift between the pump and probe when they are first separated into these two fields (Figure 3.10). We observed slight improvements to the Stokes power with tighter focusing on the probe (Figure 3.11b).
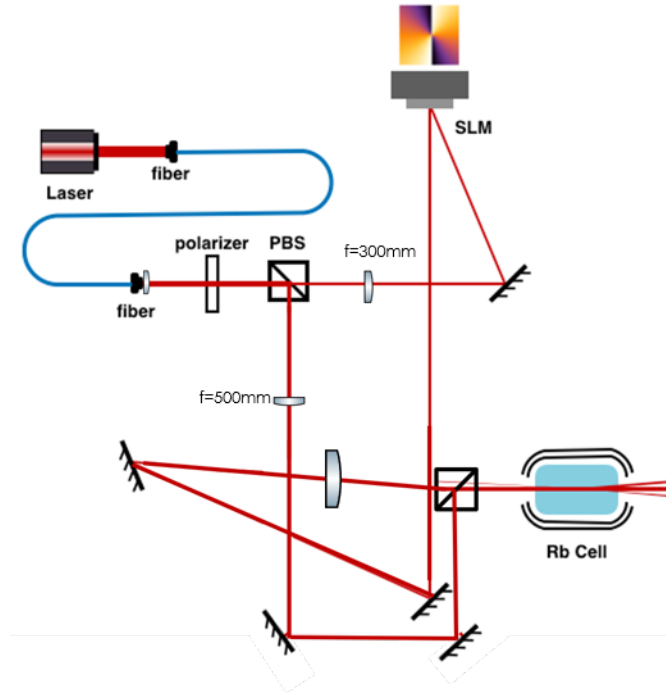
Figure 3.10: Our setup for optimizing pump and probe size. A lens on the output of our fiber coupler results in uniform phase shifts on our telescope, and the pump and probe are expanded. The probe is then focused to the center of the cell.
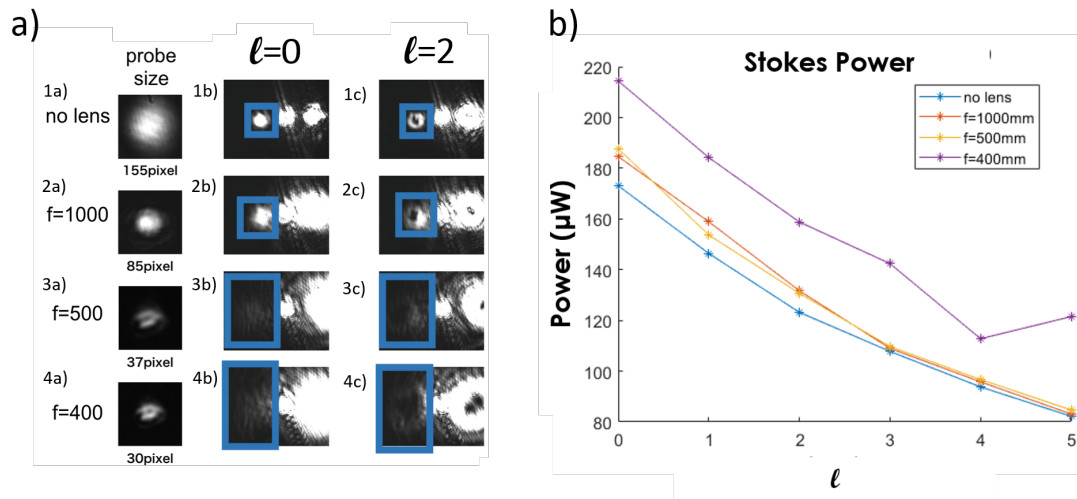
Figure 3.11: (a) Stokes produced with ℓ=0 (b) and ℓ=1 (c) probe focused to different sizes (a) at the center of the cell (where FWM occurs). (b) Stokes power with probe focused to different sizes at cell center

We also briefly explored the impact of adjusting the focus of our probe field by

using a lens on the SLM (Figure 3.12).
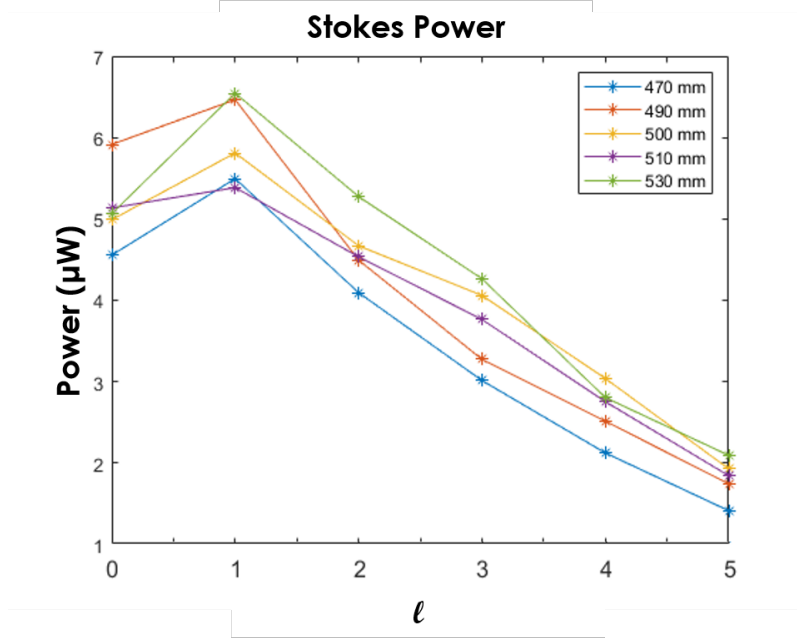
Figure 3.12: We tried to shift the focus of the probe field by applying a Fresnel lens on the SLM. However, this resulted in a significant reduction of the Stokes power without many variations to the power overall for each lens.

There were no significant changes when adjusting lens position. Additionally, since the Stokes power was much lower when using the Fresnel lens than when not using the lens, it indicated that the SLM might be altering our beam in some other way beyond the phase mask and lens focusing. It should be noted that the lens optimization occurred before the beam was profiled for any needed corrections to the phase mask. It would be interesting to explore this again with a correction to account for the beam being off center and not perfectly Gaussian.

3.6 p-Mode Generation and ℓ, p Superpositions

In addition to generating OAM in the form of ℓ modes on our fields, we successfully generated p modes (Figure 3.13) and superpositions of ℓ and p modes on our

fields (Figure 3.14). A phase mask to generate the corresponding field was applied to the SLM and generated the appropriate field on our probe. We then used the lens conditions found in the previous section to maximize four-wave mixing gain. We successfully generated Stokes fields that had OAM transfer; however, p mode transfer was at times difficult to distinguish, especially in the case with higher order superpositions of ℓ and p modes.
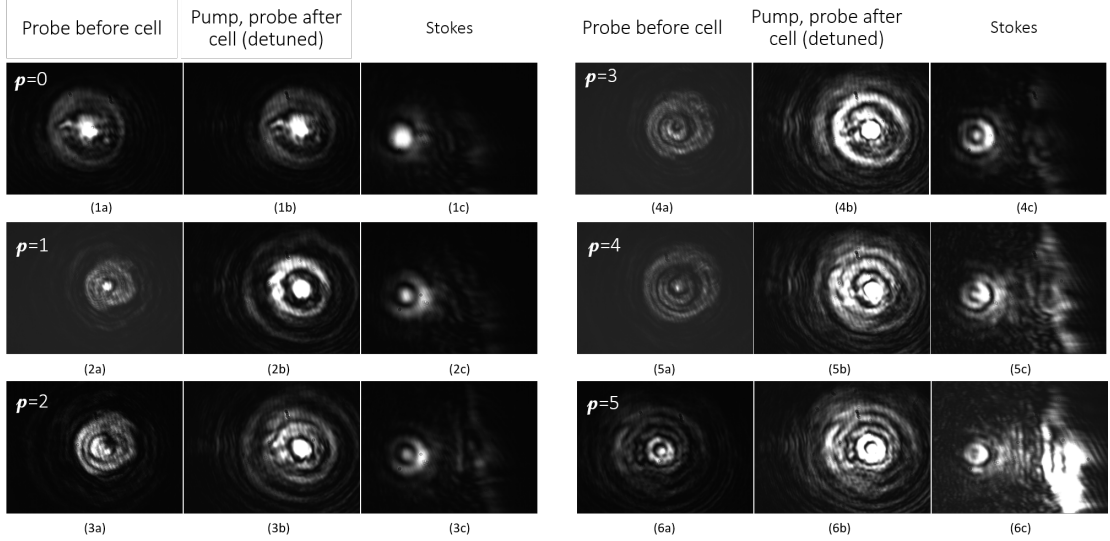
Figure 3.13: Stokes generation with $\ell = 0, p = 0, 1, 2, 3, 4, 5$. (a) The probe before the cell. (b) The pump and probe after the cell off resonance where there is no four-wave mixing. (c) The Stokes field with pump and probe blocked.

The generated Stokes field was weak compared to the amplified probe, so a razor blade was used to block the pump and probe when the Stokes image was taken to avoid over-saturating the camera.

In order to simplify the analysis of both ℓ and p mode components of our fields, superpositions of ℓ and p modes were generated by 50/50 superpositions with opposite ℓ number $(\ell, p, -\ell, p)$. Because we had a way to analyze ℓ number, but not a way to analyze p number, this meant that we could use preexisting code to confirm ℓ

mode conservation while we worked to determine p mode conservation as discussed in Chapter 4.

| Probe before cell | Pump, probe after cell (detuned) | Stokes | | Probe before cell | Pump, probe after cell (detuned) | Stokes |
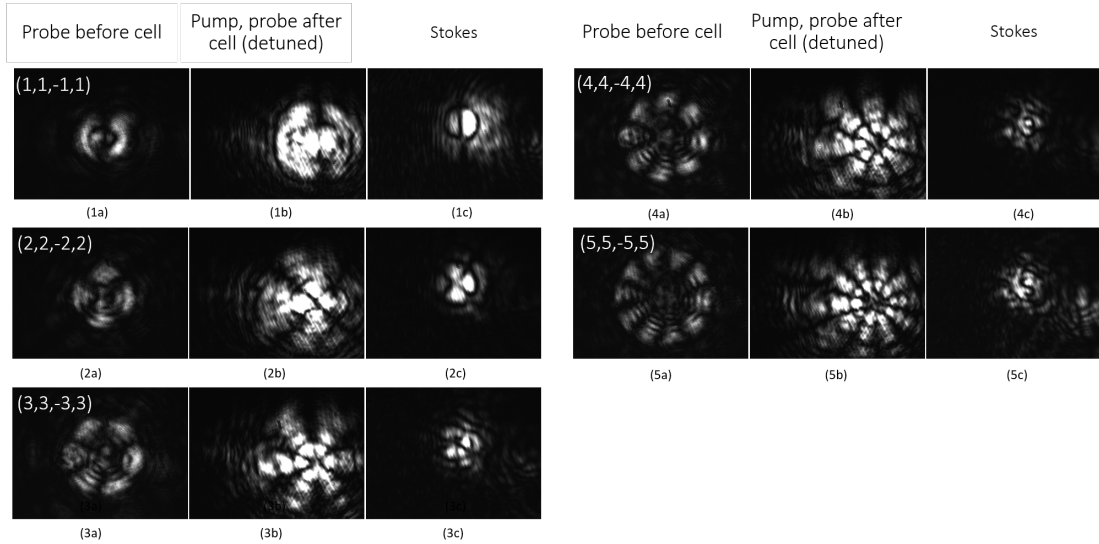
Figure 3.14: Stokes generation with 50/50 $(\ell, p, -\ell, p)$ superpositions with $\ell = p = 1, 2, 3, 4, 5$. (a) The probe before the cell. (b) The pump and probe after the cell off resonance where there is no four-wave mixing. (c) The Stokes field with pump and probe blocked.

An interesting observation was that uniformly the Stokes field seemed to be amplified more strongly on one half of the field, regardless of adjustments to phase matching conditions. This could be due to the size mismatch between the pump and probe and should be explored further. It should also be noted that the probe was being imaged in the near field on a camera placed at a distance equal to that between the lens and the center of the cell, whereas after the cell the images are taken in the far field after propagating a long distance and focused onto the camera.

Chapter 4

OAM Analysis

This chapter describes the methods of analyzing ℓ and p modes generated by our four-wave mixing setup. Because the method for analyzing ℓ modes is better understood, this chapter will focus more heavily on describing how we analyzed p mode structures.

4.1 Azimuthal Mode Analysis

Our OAM analyzer consists of a Mach-Zehnder interferometer with a Dove prism in one of the arms. The Dove prism inverts one of the beams and results in a "petal" interference pattern where the number of petals is twice the ℓ number of the beam. This is because the complex components of the generated fields add to leave only azimuthal or radial interference [15]. We can then count the ℓ numbers manually, or, for greater precision, integrate radially over the petals and fit with a Fourier series. By integrating the intensity from the center outward, we can minimize errors due to intensity fluctuations or non-uniform Stokes generation (Figure 4.2).
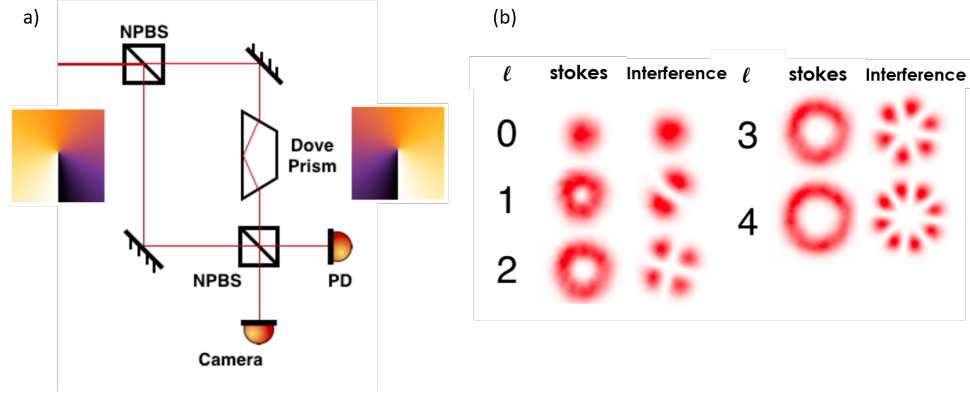
Figure 4.1: The OAM analyzer (a) allows us to more easily distinguish the OAM of our fields by studying the interference of the intensity distribution with itself. (b) Because we flip the phase with the dove prism, the interference results in "petal" structures. There are twice as many petals as there are optical phase singularities.

We are then able to conduct Fourier decomposition on the intensity profile to distinguish the structure of the beam. This is done by fitting the intensity profile over 2π radians from the center of the interference profile as shown in Figure 4.2. For lower order ℓ modes, the fit is very clear, while for higher order ℓ modes, we are able to identify the probable structure of the beam and confirm that the OAM of the probe field was transferred to the Stokes field.

Figure 4.2 1-3(a) shows the field in one arm of our interferometer. Figure 4.2 1-3(b) shows the interference pattern when the two fields are recombined, after one is rotated 90°. Figure 4.2 1-3(c) show the intensity profile of the interference pattern intensity from $-\pi$ to π radians. Figure 4.2 1-3(d) show the percentage of each Fourier component needed in order to recreate the intensity profile.
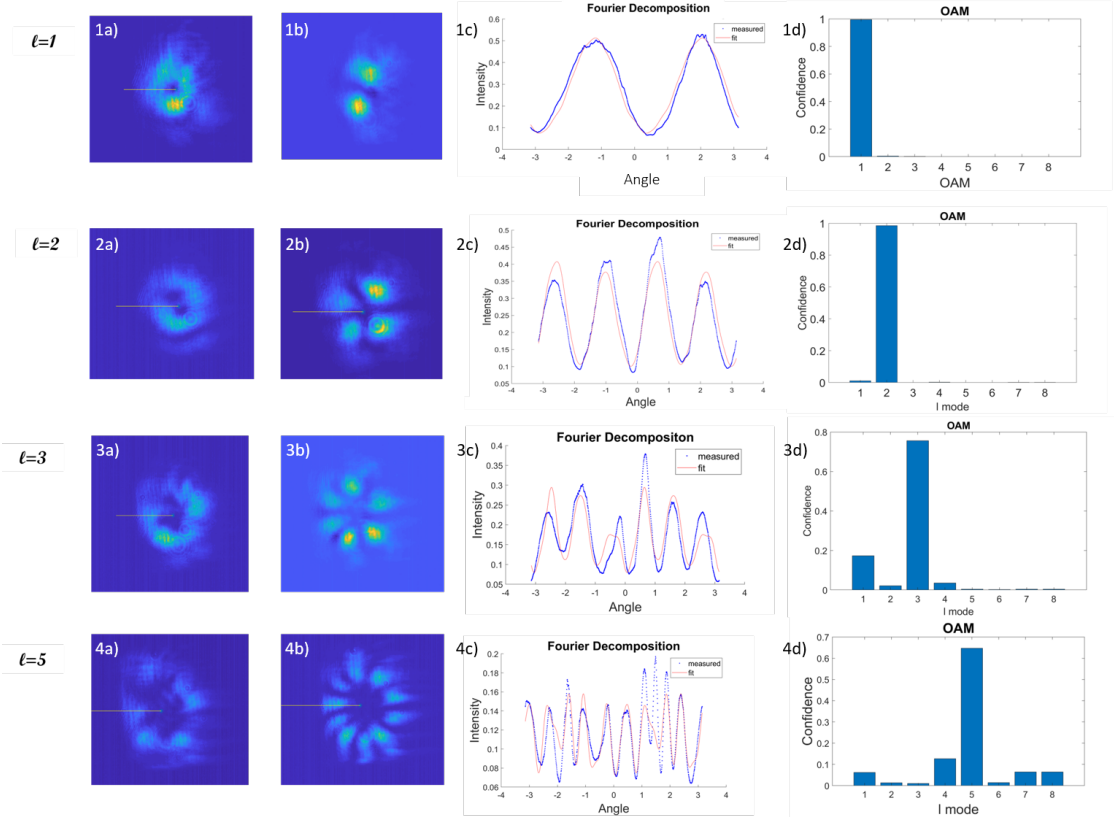
Figure 4.2: The Fourier analysis of our Stokes interference pattern for $\ell = 1$ to $\ell = 5$ (1-4). The Stokes field is shown in (a) and the interference profile is shown in (b). The intensity profile of the Stokes interference is plotted over 2π radians and fit with a Fourier series (c). The dominant oscillation frequency corresponds to the ℓ mode number (d).

We also studied four-wave mixing with superpositions of ℓ and p modes with 50/50 superpositions of $(\ell, p, -\ell, p)$ modes. It should be noted that for these fields, the OAM analyzer was not necessary because the interference of the ℓ and $-\ell$ modes in the beam resulted in the creation of the petal structures that required the use of the OAM analyzer for more simple ℓ modes (Figure 4.3).

28
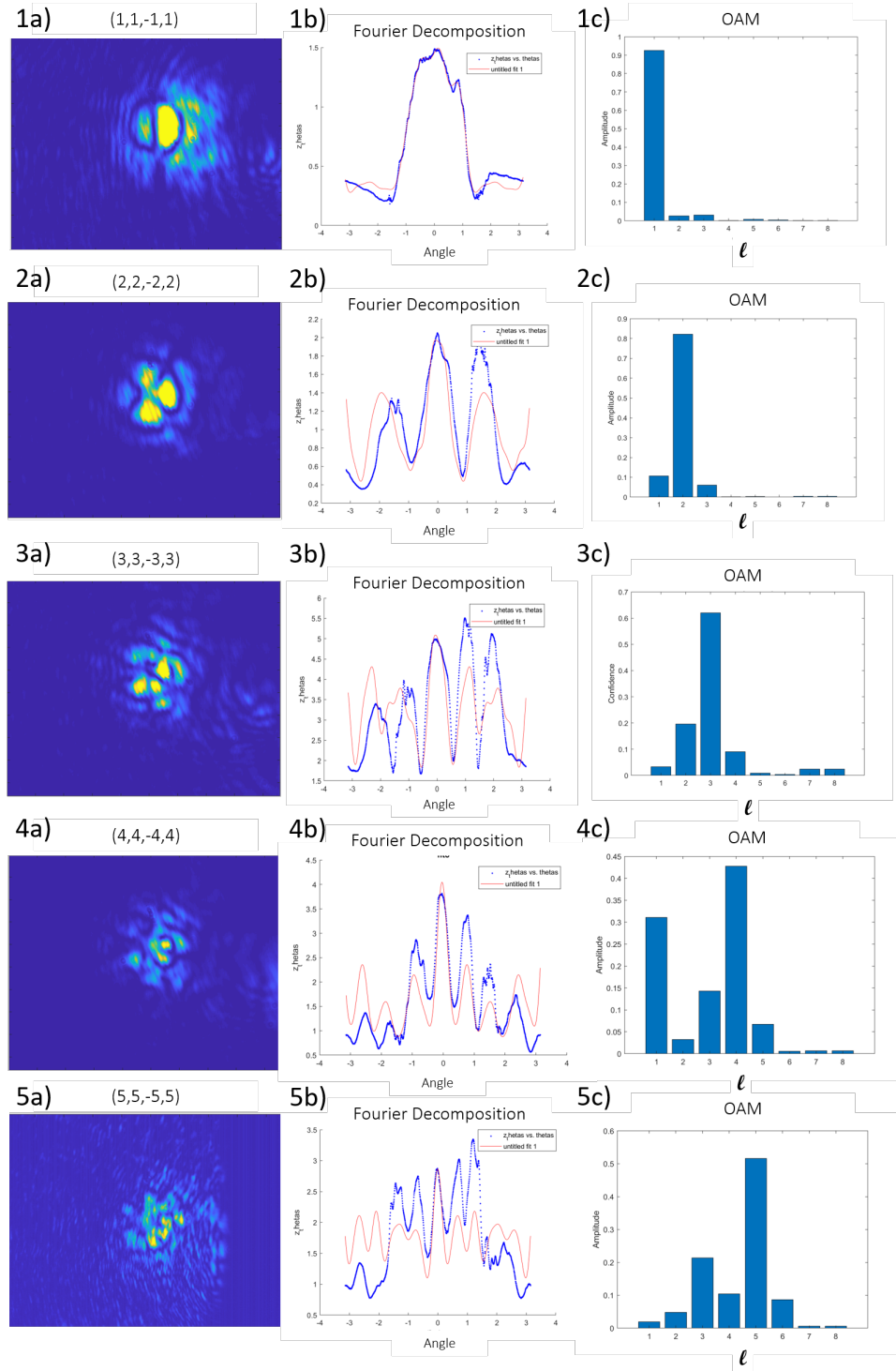
Figure 4.3: (a) Superpositions of equal ℓ and $-\ell$ modes with $\ell = p = 1, 2, 3, 4, 5$. (b) Intensity profile of petal structure and Fourier series fit. (c) ℓ index from resulting Fourier series fit.

For low order ℓ modes, it is easy to see the lobe structure for $\ell = 1, 2$. For higher order modes, it becomes more difficult to count the lobes. However, we are able to use the same methods for fitting the intensity profile to a Fourier series and can see that for $(3, 3, -3, 3), (4, 4, -4, 4)$, and $(5, 5, -5, 5)$ we fit with the expected Fourier series and can with reasonable confidence classify the mode correctly.

By doing Fourier decomposition on the beams with mode superpositions, we are able to see that ℓ number is still clearly conserved.

4.2 Radial Mode Analysis

After verifying the transfer of azimuthal ℓ modes, we then moved to studying p mode transfer. Phase masks for different p modes were applied to the probe field via the SLM. The intensity variations due to p-modes were extracted from CCD images by integrating circular cross sections from the center of the beam outward (Figure 4.4).
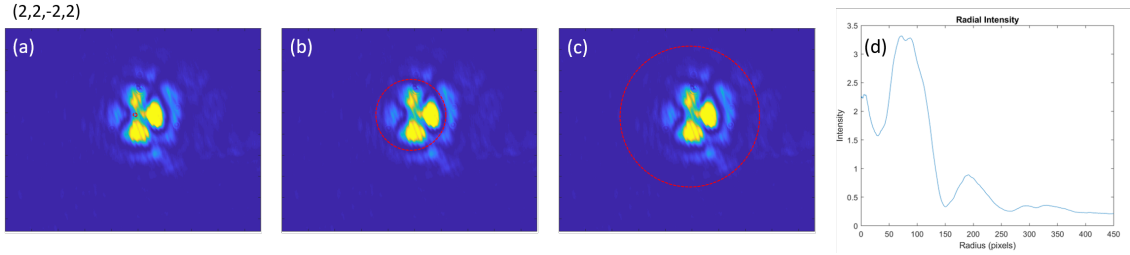
Figure 4.4: The intensity profile of p modes is taken by integrating circular cross sections of our beam starting from the center and working outward (a)→(b)→(c). The intensity profile (d) is then fit to determine the p mode structure.

Fourier decomposition yielded inconsistent results due to a decrease in intensity in outer rings. As a result, ideal beams simulated by Kangning Yang were used to fit our data. Since we required the use of a lens to capture the entire Stokes field on the camera, simple linear regression often failed because the location and size of

each ring was compressed. We ultimately decided to use wavelets created from the simulated data to conduct our fits.

4.2.1 Linear Regression

All of our fits were done with simple linear regression, either using the radial intensity of the simulated fields or wavelets created from them. This was of the form

$$\hat{I}_{meas} = \beta_1 I_1 + \beta_2 I_2 + \beta_3 I_3 + \beta_4 I_4 + C \tag{4.1}$$

where I_{meas} is the measured radial intensity, I_1, I_2, I_3, I_4 are the radial intensities corresponding to simulated fields with $p = 1$, $p = 2$, $p = 3$, and $p = 4$, $\beta_1, \beta_2, \beta_3, \beta_4$ are fit coefficients, and C is a constant to account for any background. The simulated intensities were fitted to each experimental field by choosing coefficients that minimized the mean square error,

$$MSE = \frac{1}{n} \sum_{i=1}^{n=1000} (I_i - \hat{I}_i)^2 \tag{4.2}$$

where n is the total number of data points in our intensity curve (1000), I_i is the actual measured intensity, and $\hat{I}_i$ is the fitted value of the intensity curve.

4.2.2 Ideal Fitting Fields

We explored two different types of candidates to conduct our fits: fields with $\ell = 0$, p=1,2,3,4 and fields with a 50-50% superposition of ℓ and p modes (ℓ,p,$-\ell$,p) such that $\ell = p$.
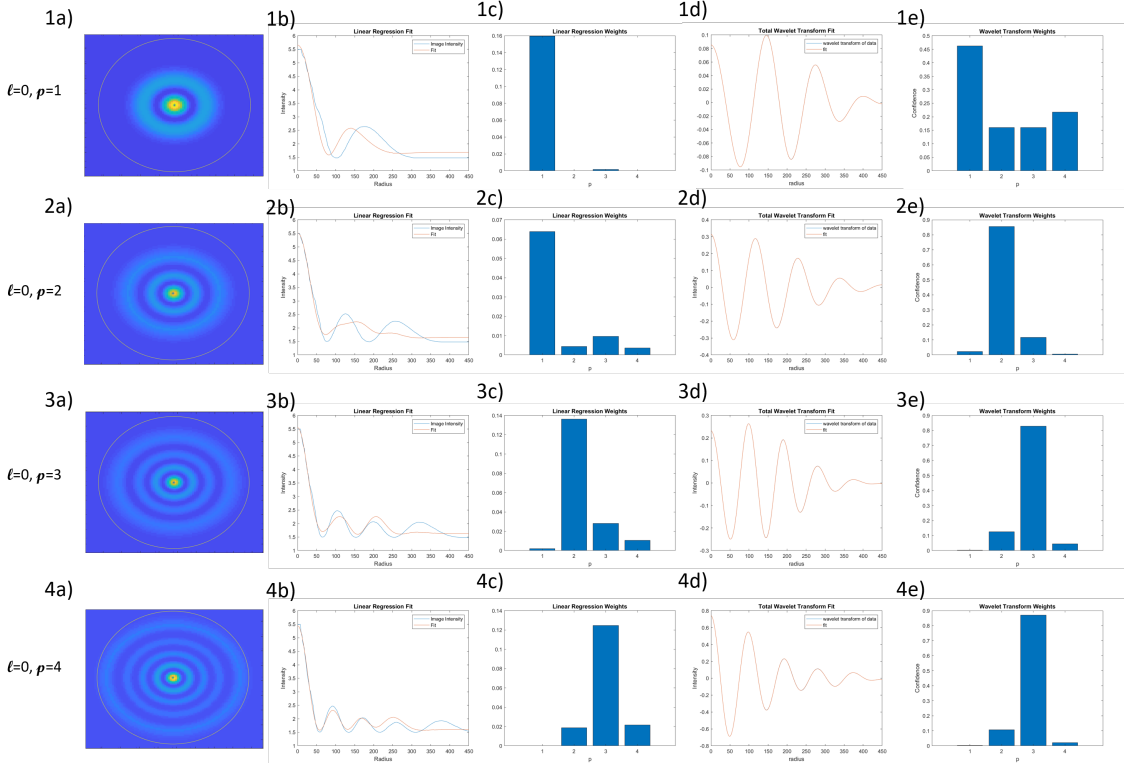
Figure 4.5: The (a) intensity profiles for simulated beams with $\ell = 0$, p=1,2,3,4 recorded. The data for all four fields were then used to fit each individual intensity curve to determine a baseline accuracy of our method. (b) Linear regression yielded fits that varied from the actual value, and (c) the components of the fit did not correspond to the actual mode. Additionally, when (d) conducting regression with wavelets, while we were able to reconstruct the wavelet profile of the beam, these components (e) also deviated significantly from the given mode.

We would expect perfect or near-perfect fitting of the simulated data because we were checking the accuracy of the linear regression and wavelet transform methods for fitting our data with the same dataset we used to build it. However, due to similarities in the $(\ell = 0, p)$ fields, both linear regression and wavelet analysis yielded fits that did not correspond to the ideal optical mode (Figure 4.5).

We then explored beams constructed from a superposition of ℓ and p modes as a fitting option (Figure 4.6).
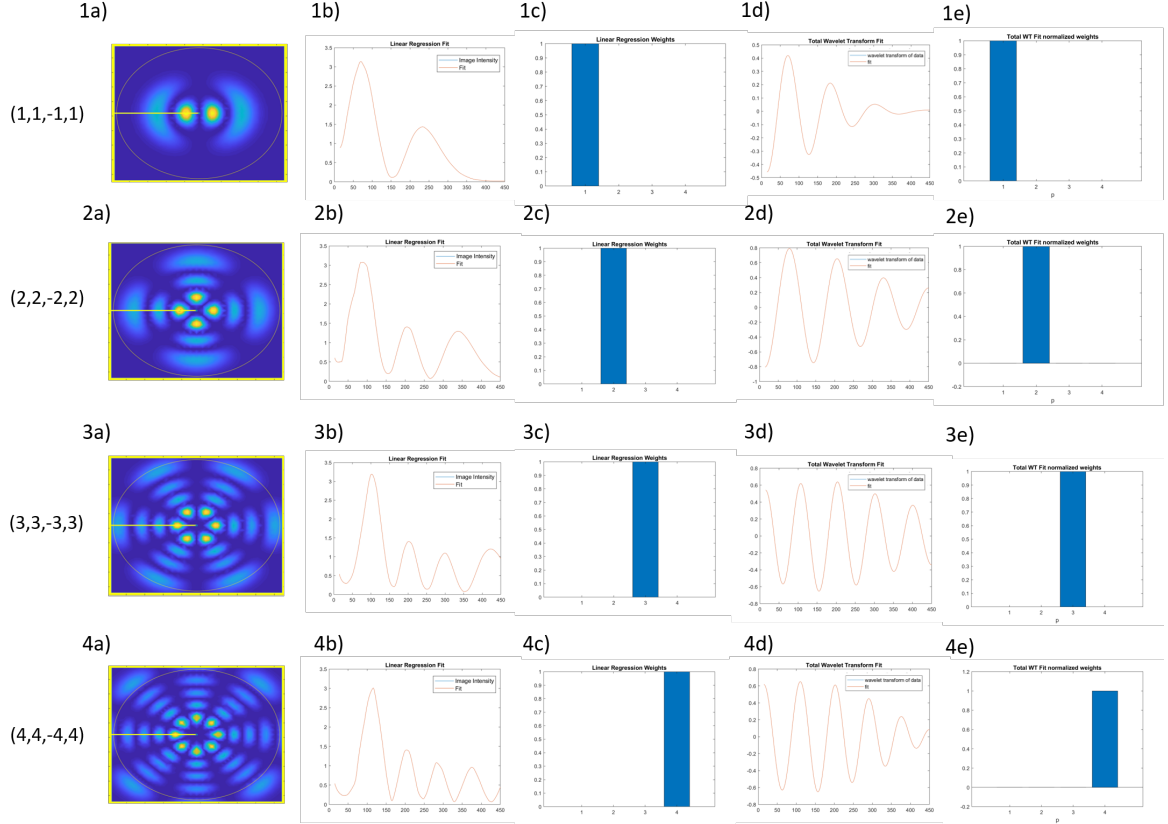
Figure 4.6: (a) Simulated 50-50 superpositions of fields of the form $(\ell, p, -\ell, p)$ with $\ell = p = 1, 2, 3, 4$. The radial intensity of the fields was used to construct fits. The accuracy of this fit was then initially tested with (a) linear regression and (d) wavelet transformations. Since the fits indicated the expected p modes for both (c) regular linear regression and (e) linear regression with wavelets, we elected to conduct our fits with the beams created from the asymmetric mode superpositions.

Because there were significant improvements to both fitting methods using a superposition of ℓ and p modes and the intensity and frequency components of each mode were more distinct, we elected to use the superposition modes for our fits.

4.2.3 Linear Regression

Linear regression was done on both simulated fields with $\ell \neq p$ (Figure 4.7) and experimental fields for $\ell = 0, p$ modes (Figure 4.8) and anti-symmetric $(\ell, p, -\ell, p)$ superpositions (Figure 4.9). Changes in beam position between the simulated and

experimental fields was accounted for by manually selecting the center of each beam. However, changes in beam size could not be accounted for with simple linear regression.
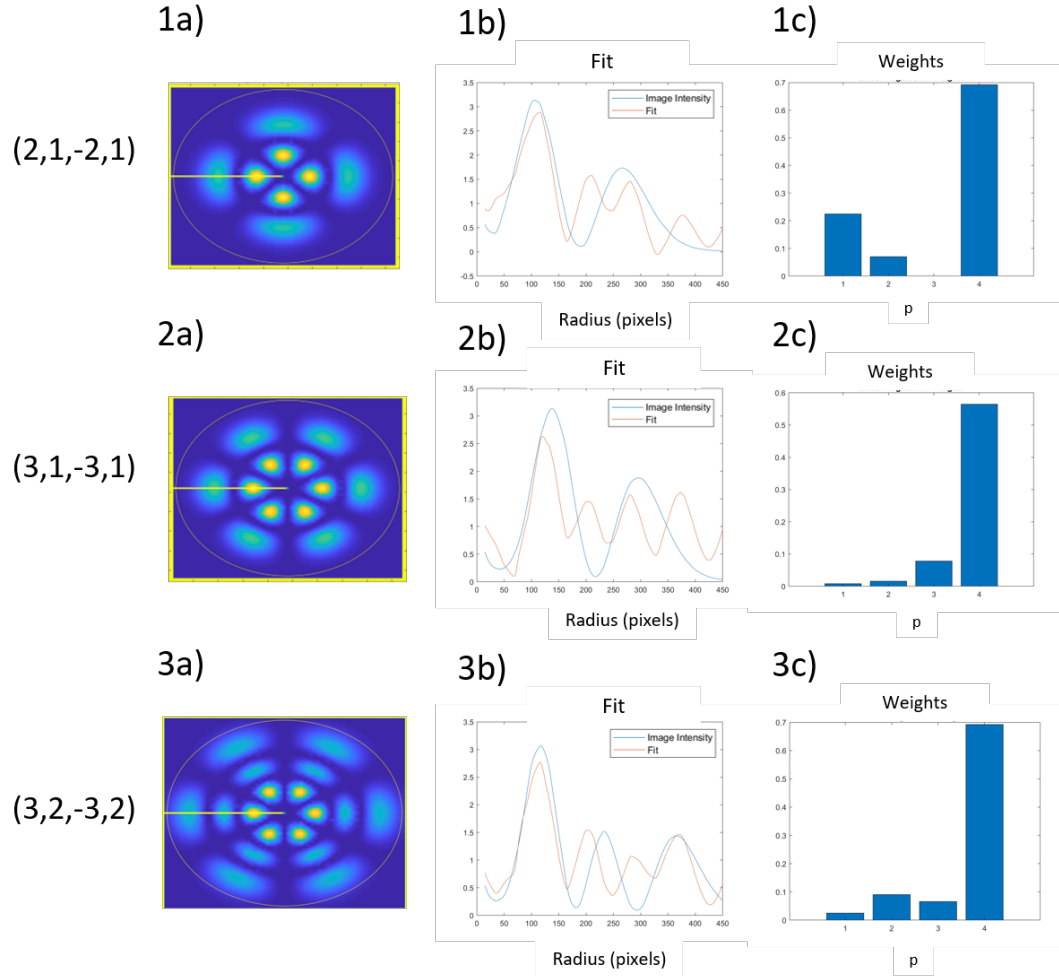
Figure 4.7: (a) Simulated stokes field for (2,1,-2,-1), (3,1,-3,1), and (3,2,-3,2) superpositions. (b) The radial intensity of the fields and fit using linear regression. (d) Proportion of each p-mode fit in the linear regression fit.

The simulated $(\ell, p, -\ell, p)$ mode superpositions did not yield a fit indicating the expected p mode using linear regression. In fact, it was almost uniformly determined that all Stokes fields were composed of primarily the $p = 4$ mode in order to yield the minimum average error due to the fluctuations in the field intensity.

34
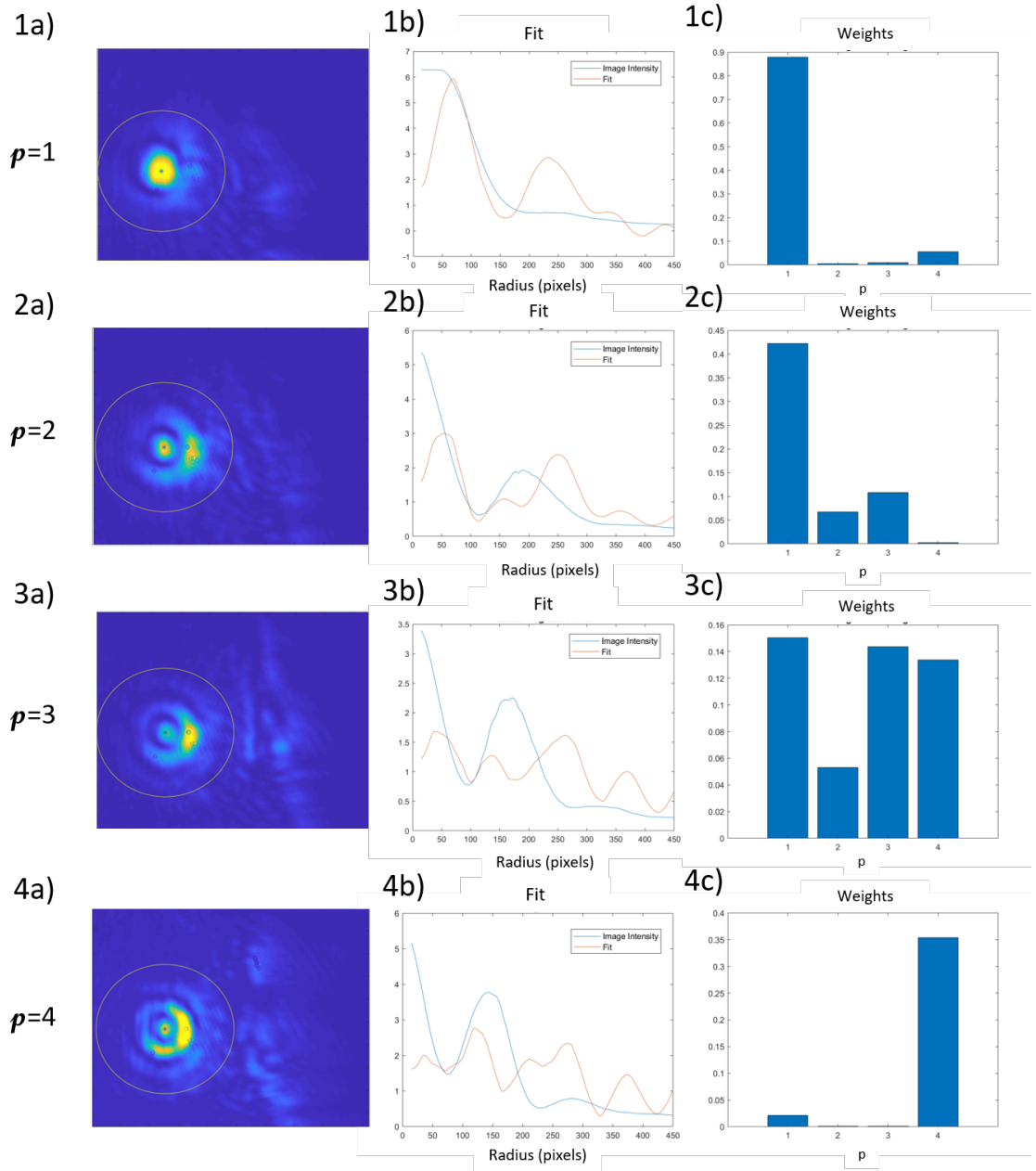
Figure 4.8: (a) Experimental Stokes field for $\ell = 0, p = 1, 2, 3, 4$. (b) The radial intensity of the field and linear regression to fit it using simulated data. (c) Proportion of each p-mode in the linear regression fit.

The experimental $\ell = 0, p$ fields did not yield a fit indicating the expected p mode using linear regression. While the expected result was obtained for $p = 1$ and $p = 4$, the fit deviated substantially from the actual intensity and the predicted value for

$p = 2, 3$ deviated from the expected value.
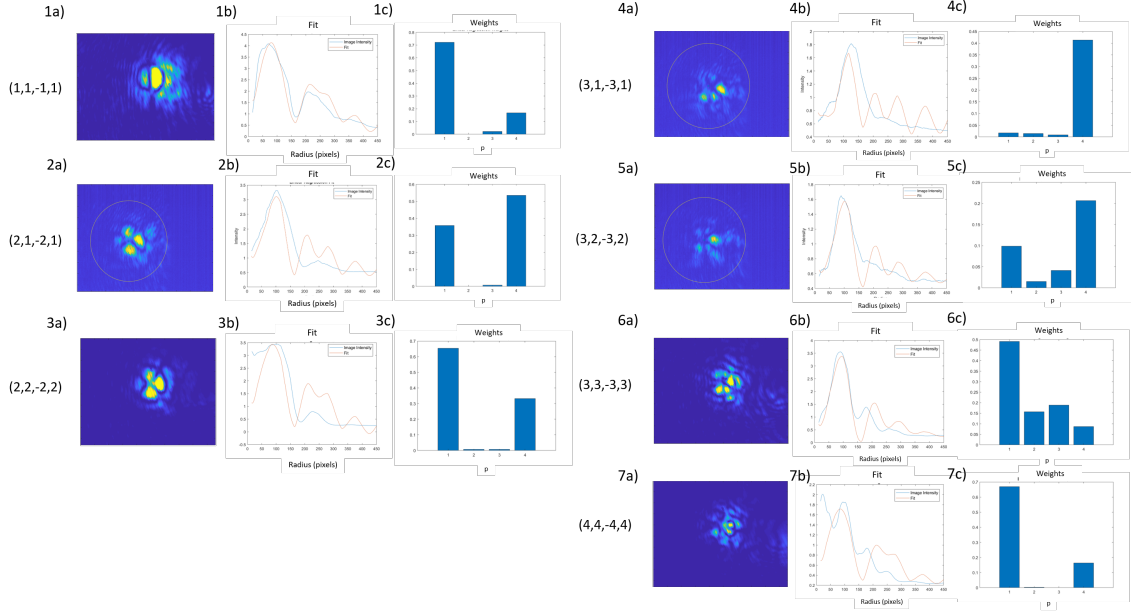
Figure 4.9: (a) Experimental Stokes field for $(\ell, p, -\ell, p)$ superpositions. (b) The radial intensity of the field and linear regression to fit it using simulated data. (c) Proportion of each p-mode in the linear regression fit.

The experimental $(\ell, p, -\ell, p)$ superpositions yielded a fairly accurate fit for $(1, 1, -1, 1)$. However, this is not true for any of the other superpositions, where we had very inaccurate fits and p mode predictions that deviated from what we expected.

Since we had large errors and unexpectedly poor results from fitting with linear regression, we ultimately decided to explore the use of wavelets for fitting our data since this would allow us to change the scaling for different beam sizes.

4.2.4 Wavelet Analysis

Wavelets are used as an alternative to Fourier transformations because they provide more localized spatial and frequency information so we can produce a spectrum of wavelets, rather than a single Fourier transformation [17]. Similar to the Fourier

transformation, they take the inner product between a signal and an analyzing function, called the "mother wavelet" in order to analyze the components in both the time and frequency domains. This allows us to construct a 2D representation of the signal so we can shift, stretch, and compress it. It was determined that this method was advantageous to Fourier decomposition when analyzing p-modes due to changes in intensity for rings further from the center of the beam and changes to minima and maxima position with changes to ℓ number.

Mother wavelets can be constructed from a function ψ such that

$$c_\psi = 2\pi \int_{-\infty}^{\infty} \frac{|\Psi(\omega)|^2}{|\omega|} d\omega < \infty \tag{4.3}$$

where $\Psi(\omega)$ is the Fourier transformation of our data, ψ. Our data analysis was conducted in MATLAB, and as a result our mother wavelet is the Morse wavelet [18]. The transformation of the signal is defined as

$$S(b,a) = \frac{1}{\sqrt{a}} \int_{-\infty}^{\infty} \psi'\left(\frac{r-b}{a}\right) s(r) dr \tag{4.4}$$

where Ψ' is the complex conjugate of the Morse wavelet and $s(r)$ is the signal, defined for $b \in \mathbb{R}$ and $a > 0$. b gives the time shift of the wavelet and a the scalar shift of the wavelet. The Fourier transformation of the Morse wavelet is defined as

$$\Psi_{\beta,\gamma}(\omega) = U(\omega) a_{\beta,\gamma} \omega^\beta e^{-\omega^\gamma} \tag{4.5}$$

where $U(\omega)$ is the heaviside step function and

$$a_{\beta,\gamma} \equiv \left(\frac{e\gamma}{\beta}\right)^{\beta/\gamma} \tag{4.6}$$

is a normalizing constant [19] We can thus define

$$\psi_{a,b}(r) = \frac{1}{\sqrt{a}} \psi\left(\frac{r-b}{a}\right) \tag{4.7}$$

37

and we can reconstruct the transformation

$$S(b,a) = \int_{-\infty}^{\infty} \psi'_{a,b}(r)s(r)dr \qquad (4.8)$$

The original signal can thus be reconstructed as

$$s(r) = \frac{1}{c_\psi} \int_{-\infty}^{\infty} \int_{-\infty}^{\infty} S(b,a)\psi_{a,b}(r)\frac{dadb}{a^2} \qquad (4.9)$$

Most importantly for our data, the wavelet transformation can identify phase ridge points of the signal in time and space along which there is an inflection point [20]. This allows us to identify where maxima and minima are occurring, even if we have very low signal intensity. The scaling of wavelets is shown in Figure 4.10.
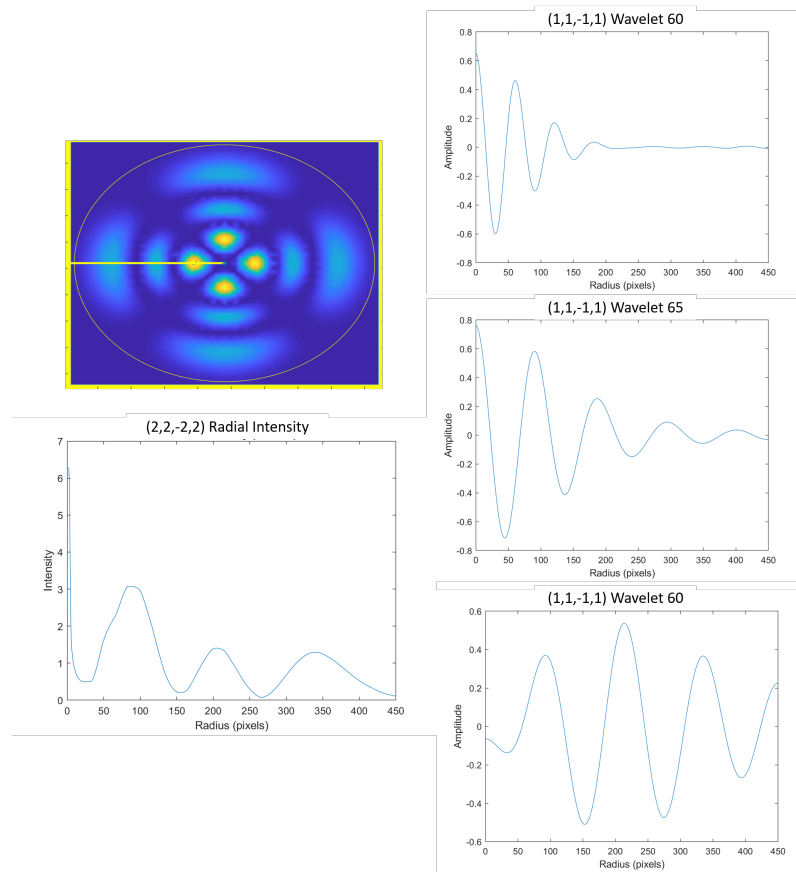
Figure 4.10: (1,1,-1,1) superposition wavelet transformations with different scalings. As the scaling is increased, the wavelet is both stretched and compressed.

In order to construct our fit, a continuous wavelet transform was conducted on simulated data provided by Kangning Yang (Figure 4.11). This allowed us to identify the frequency components and how p-mode intensity changed from the center of the beam outwards in rings.
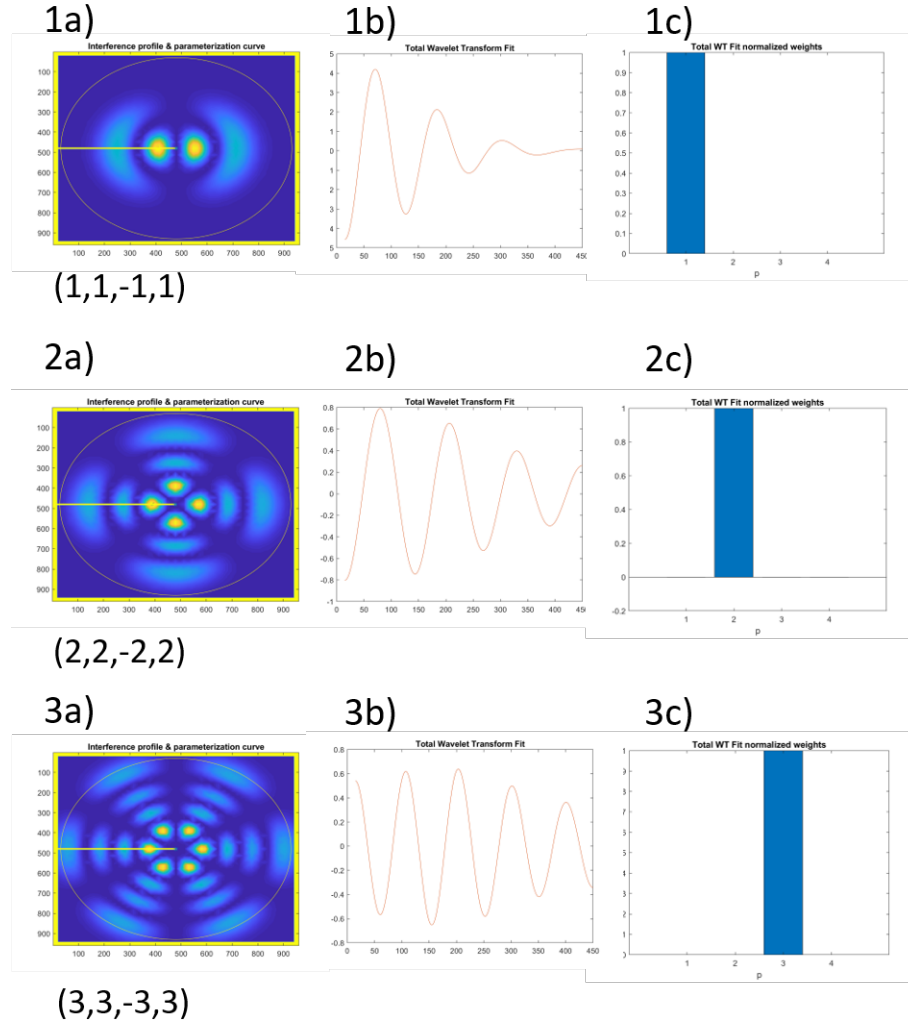
Figure 4.11: Simulated superpositions of ℓ and p modes with $|\ell| = p = 1, 2, 3$. (a) shows the simulated intensity profile, (b) shows one wavelet transform and (c) shows the p number.

This was used to create a basis for linear regression using the wavelet transformation. The experimental data was converted into a wavelet and a wavelet coefficient

was selected to ensure that all features were present in the converted data set. We then used wavelets for $p = 1, 2, 3, 4$ with 71 different coefficients for each wavelet grouping in order to fit the data with changes to peak positions and intensities.

The coefficients for each collection of wavelets are then summed and normalized in order to determine the main components of experimental data such that

$$\Psi_{meas} = \beta_0 + \sum_{p=1}^{4} \sum_{w=1}^{71} \beta_{pw} \Psi_{pw}(r) \tag{4.10}$$

where β_0 is a constant background, p is the radial index, w is the wavelet coefficient, β_{pw} is the fitting parameter for a given wavelet f_{pw} at mode p and wavelet scaling w. Fit coefficients were chosen with general linear regression using the wavelets in order to minimize the mean square error (Equation 4.2)

The accuracy of our fit was once again tested on simulated superpositions of $\ell \neq p$ $(\ell, p, -\ell, p)$ modes (Figure 4.12) and experimental data for $\ell = 0, p$ (Figure 4.13) and $(\ell, p, -\ell, p)$ modes (Figure 4.14).
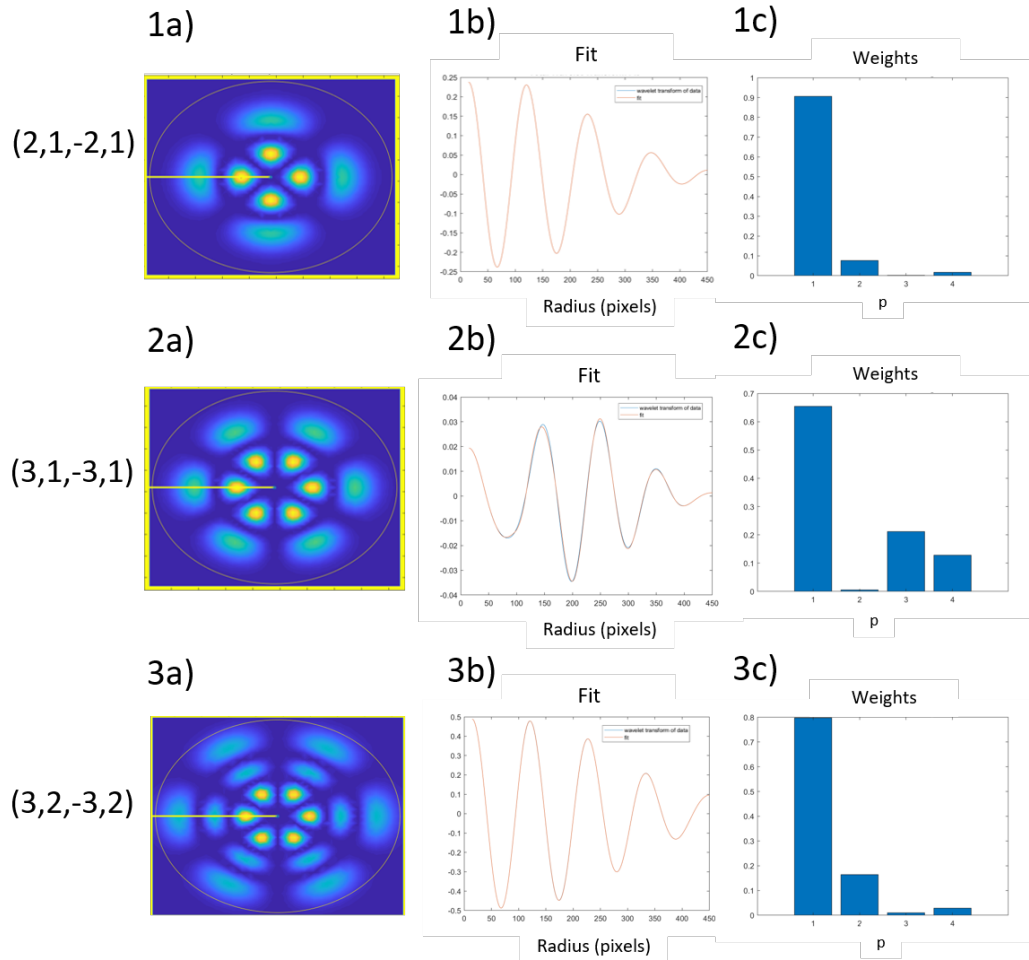
Figure 4.12: Wavelet transform analysis for (a) simulated $(\ell, p, -\ell, p)$ superpositions where $\ell \neq p$. (b) The radial intensity is determined, transformed into a wavelet, and then fitted with wavelets from simulated $(\ell, p, -\ell, p)$ fields where $\ell = p$. (c) proportion of each p in the fit.

Wavelet fitting was successful in fitting superposition fields with $p = 0$. However, for $(3, 2, -3, 2)$, the p mode component was identified as $p = 1$ rather than $p = 2$ while we had a very low mean square error and high r^2 value.
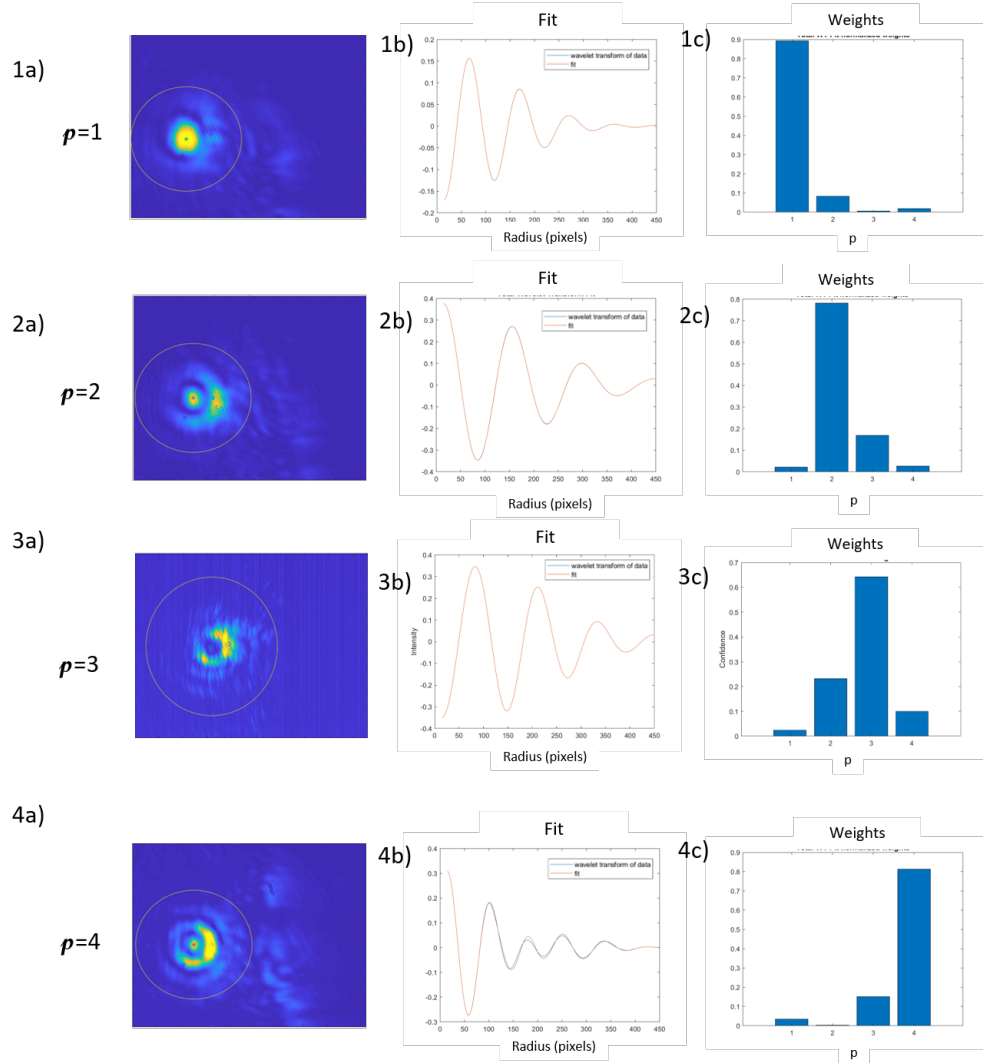
Figure 4.13: (a) Stokes field with $p = 1, 2, 3$ and 4. The intensity of the Stokes field is integrated from the center to the edge of the field and transformed into wavelets. (b) One wavelet is then selected to be fit with the simulated wavelets with linear regression. (c) The weights for each simulated wavelet in the linear regression are then normalized to determine the confidence of each OAM classification.

We obtained a high fit confidence for $p = 1, 2, 3$, and a reasonably high confidence for $p = 4$. However, it should be noted that for larger p numbers, there seem to be an increase in other modes identified in the field.
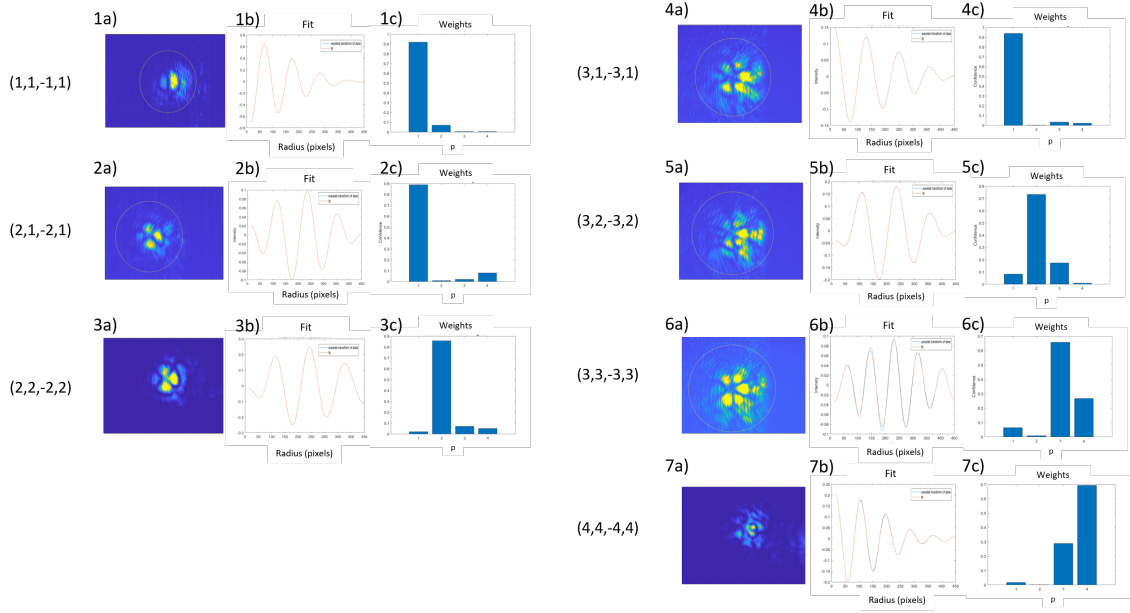
Figure 4.14: Wavelet transform analysis for (a) $(\ell, p, -\ell, p)$ superpositions where $\ell \neq p$. (b) The radial intensity is determined, transformed into a wavelet, and then fitted with wavelets from simulated $(\ell, p, -\ell, p)$ fields where $\ell = p$. (c) proportion of each p in the fit.

Our wavelet transformation fitting method was reasonably successful in identifying the p mode components of our experimental fields. As the ℓ and p numbers increased, we once again saw an increase in other p modes being present in the components of our field.

Chapter 5

Results and Conclusions

5.1 Conclusion and Future Plans

We have achieved four-wave mixing with OAM transfer, in which azimuthal and radial modes were transferred from the probe field to the generated Stokes field. We have also determined focusing conditions for optimal Stokes field generation and methods for characterizing both ℓ and p modes. As a result, we have confirmed that ℓ modes transfer is conserved during the four-wave mixing process. While we are able to characterize p modes generated via four-wave mixing, it has been observed that p mode transfer requires an appropriate pump to probe size ratio and resolution is lost at higher p numbers.

However, it would be worthwhile to spend more time developing p mode analysis. There are some questions and inconsistencies that arise as a result of using wavelets to do linear regression. Since we are analyzing how the frequency components change in space and scaling each wavelet accordingly, we are able to yield fits that agree with expected values. However, this is done only after a wavelet is selected from the experimental data. Changes to the selected wavelet scaling can result in significant changes to the fit (although scaling with no compression or with limited compression

typically yields optimal results). This raises questions on the accuracy of the wavelet fitting method in the case that we do not know the target p mode.

Additionally, we have not completed this analysis with superpositions of different p modes, and in this case it is likely that we will need to develop a new method to do this analysis. It would also be useful to confirm our results with (ℓ_1, p, ℓ_2, p), $\ell_1 \neq \ell_2$ superpositions to determine if the analysis would be useful with this case.

For these reasons, it could be interesting to develop a mode sorting method that is not purely analytical such as explored by Zho and Fontine, et. al. [21], [22]. We could also implement a tilted lens projection from circularly symmetric Laguerre-Gaussian modes to rectangularly symmetric Hermite Gaussian modes [23] to simplify the analysis of our different mode components.

Finally, we are interested in exploring the introduction of a second pump field to study Stokes generation with two pump inputs, rather than just one. We expect this to result in a Stokes generated in the opposite direction, and it would be interesting to determine OAM transfer and conservation in this case.

Chapter 6

Public Abstract

6.1 Introduction and Background

Conventional computer systems send information as electric signals. These signals, called bits, switch on and off in order to convey a message. The message speed depends on how fast electrons can move through a cable. However, it is possible to use light instead of electrons to send more information at once and send that information faster. This is because, rather than sending signals based on the presence of electrons, we can store information in the amplitude and phase of light. Light can carry orbital angular momentum (OAM) which can be used to transmit information even more efficiently by encoding each photon with different OAM to give each signal a different meaning [2]. Additionally, entangled quantum states can be used to prevent eavesdropping because any unauthorized measurement will affect the system. This results in a low error threshold that requires the receiver to know how to properly measure the system in order to be able to understand the message [3].

During my undergraduate research, I have demonstrated that information can be encoded into beams of light via OAM and that this information can be transferred to a new field via a nonlinear interaction due to energy and momentum conservation. This

interaction is called four-wave mixing (FWM). Since FWM results in the generation of a new field correlated with an input field, any disruptions between them will result in a loss of information that protects the sender.

6.2   Summary of Results

We have successfully demonstrated four-wave mixing with OAM transfer up to $\ell = 5$, $p = 5$ by applying phase masks to the probe beam using a spatial light modulator. We have optimized temperature, focusing, and cell conditions. Furthermore, we have demonstrated mixing with OAM conservation for superpositions of ℓ and p modes. A new method for p mode analysis using wavelets has been developed and is described in this work.

6.3   Intellectual Merit

This research has the potential to make groundbreaking advances in quantum information and quantum computing. I hope to further improve the understanding of nonlinear optics and how it can be used to more effectively send information. I hope that my research will make substantial advancements in the field of quantum information while also improving modern information systems and security.

6.4   Broader Impact

This technology will allow for faster, safer communication and distribution of information. It will make banking, military, and individual communications more secure because eavesdroppers will be unable to interpret the signals. Technology is continuously advancing into the quantum realm. As a result, it is important to expose the general population to quantum phenomenon so they can understand new technology. I hope by creating a robust and secure method of information distribution and

deliberate outreach efforts I will be able to make meaningful advances in increasing the general knowledge base surrounding quantum optics.

Bibliography

[1] Paschotta, R. *Optical Fiber Communications.* RP Photonics Encyclopedia.

[2] Erhard, M, Fickler, R., Krenn, M., & Zeilinger, A. *Twisted photons: new quantum perspectives in high dimensions.* Nature, 7(17146). (2017).

[3] Yang, L., Wen-Hong, Z., Cun-Lin, Z., & Gui-Lu, L. *Quantum Computation with Nonlinear Optics.* Communications in Theoretical Physics, 49(107) (2008).

[4] Thiel, C.W. *Four-Wave Mixing and its Applications.* A. Atomic Physics and Spectra, CARS.

[5] Altmann, Y., McLaughlin, S., Padgett, M. J., Goyal, V. K., Hero, A. O., & Faccio, D. *Quantum-Inspired Computational Imaging.* Science, 361(6403) (2018). doi:10.1126/science.aat2298

[6] Meyers, R. E., & Deacon, K. S. *Space-Time Quantum Imaging.* Entropy, 17(3), 1508-1534 (2015). doi:10.3390/e17031508

[7] Lemos, G. B., Borish, V., Cole, G. D., Ramelow, S., Lapkiewicz, R., & Zeilinger, A. *Imaging via Quantum Indistinguishability of Undetected Photons.* Research in Optical Sciences, 512, 409-412 (2014). doi:10.1364/qim.2014.qtu1a.1

[8] Genovese, M. *Real Applications of Quantum Imaging.* Journal of Optics, 18(7), 1-10 (2016). doi:10.1088/2030-8978

[9] Hanna, D. C., Cotter, D., & Yuratich, M.A. *Nonlinear Optics of Free Atoms and Molecules.* Springer-Verlag Berlin Heidelberg 17 (1979).

[10] Mills, D.L. *Nonlinear Optics: Basic Concepts.* Springer-Verlag Berlin Heidelberg (1991)

[11] Banerjee, P.P. *Nonlinear Optics: Theory, Modeling, and Applications.* CRC Press (2003).

[12] Roman, K. *Entangling Photons via Four-Wave Mixing in a Rubidium Vapor Cell.* William & Mary Undergraduate Thesis (2015).

[13] Barnett, S.M., Babiker, M., & Padgett, M.J. *Optical orbital angular momentum.* Philosophical Transactions of the Royal Society A: Mathematical, Physical and Engineering Sciences (2017).

[14] Prajapati, N., Super, N., Lanning, R.N., Dowling, J.P., & Novikova, I.]textitOptical Angular Momentum manipulations in a Four Wave Mixing Process. Optics Letters 44(4). (2019).

[15] Offer, R.F., Stulga, D., Riis, E., Franke-Arnold, S., & Arnold, A.S. *Spiral bandwidth of four-wave mixing in Rb vapor.* Communications in Physics 1 (2018).

[16] Offer, R.F., Stulga, D., Riis, E., Franke-Arnold, S., & Arnold, A.S. *Spiral bandwidth of four-wave mixing in Rb vapour.* Nature Communications Physics 1(84) (2018).

[17] Lee, D. T. & Yamamoto, A. *Wavelet Analysis: Theory and Applications.* Hewlett-Packard Journal (1994).

[18] *Morse Wavelets* TheMathWorks, Inc. (1994-2020).

50

[19] Lilly, J.M & Olhede, S.C. *Higher-Order Properties of Analytic Wavelets* IEEE Transactions on Signal Processing, 57(1), 146-160 (2009).

[20] Lilly, J.M. & Olhede, S.C. *On the Analytic Wavelet Transform* IEEE Transactions on Information Theory, 56(8), 4135-4156 (2010).

[21] Zhou, Y., Mirhosseini, M., Fu, D., Zhao, J., Rafsanjani, S.M.H., Willner, A.E., & Boyd, R. *Sorting Photons by Radial Quantum Number* Physical Review Letters 119(263602), 1-5 (2017).

[22] Fontine, N., Ryf, R., Chen, H., Neilson, D., & Kim, K. *Laguerre-Gaussian mode sorter* SPIE 10935, Complex Light and Optical Forces XIII, 1093512 (2019).

[23] Berkhout, G.C.G., Laverly, M.P.J., Courtial, J., Beijersbergen, M.W., & Padgett, M.J. *Efficient Sorting of Orbital Angular Momentum States of Light* Physical Review Letters 105(153601) 1-4 (2010).